

ARISTOTLE UNIVERSITY OF THESSALONIKI

Finite element image reconstruction in microwave ablation treatment

Konstantinos Katrioplas

Supervisor: Prof. Theodoros Samaras

Master's Degree in Computational Physics
Department of Physics

February, 2017

Abstract

Finite element image reconstruction in microwave ablation treatment

by Konstantinos Katrioplas

Reliable imaging of biological tissues during microwave ablation is crucial to the effect of cancer treatment. Real time evaluation of the ablated area is based upon the change of the dielectrical properties of the surrounding tissue. In silico electrical impedance tomography (EIT) is used to reconstruct images of a 26-year old realistic human model during a 10-minute treatment at 2.45 GHz. In place of real voltage measurements, the electrostatic field is solved using the FEM. Gauss-Newton reconstruction algorithm is implemented to obtain images via the open source numerical suite EIDORS. Simulation results evidence the possibility of real-time image reconstruction using EIT. Average electrical conductivity value of the tumor area indicates an error of less than 5% of the assumed value at the end of the treatment.

Contents

Abstract	iii
1 Motivation	1
1.1 Mechanisms of tumour cell death	1
1.1.1 Radiofrequency ablation	2
1.1.2 Microwave ablation	4
1.1.3 Dielectric properties during MWA treatment	5
1.1.4 Regression modeling for dielectric properties in MWA	8
1.2 Imaging techniques	9
1.2.1 Electrical Impedance Tomography	10
2 The finite element method	13
2.1 The static electrical field	13
2.1.1 Weak formulation	14
2.1.2 The Galerkin approximation	15
2.2 Implementation	16
2.2.1 Shape functions	17
2.2.2 Jacobian transformation	18
2.2.3 Assembly	20
2.3 Solution of discrete system	22
2.4 Validation	23
3 Image Reconstruction	27
3.1 Inverse problem in EIT	27
3.2 Reconstruction algorithm	28
3.2.1 General statement of the problem	28
3.2.2 Non-linear least squares	28
3.2.3 Gauss–Newton algorithm	30
3.2.4 Tikhonov regularization	31

3.2.5	Noser regularization	32
3.2.6	Application in 3D EIT	32
4	Results	33
4.1	Human models	34
4.1.1	Virtual population	34
4.1.2	Mesh	34
4.2	Model design	35
4.2.1	Electrodes placement	35
4.2.2	Target area properties	36
4.3	Reconstruction results	38
4.3.1	Forward solution	38
4.3.2	2D reconstruction	38
4.3.3	Single instance reconstruction	42
4.3.4	Multiple reconstruction during ablation	42
5	Discussion	45
5.1	On the forward problem	45
5.2	On the model design	46
5.3	On the reconstructed image	47
	Bibliography	53

List of Figures

1.1	The zones of hyperthermic ablation	3
1.2	Electric field polarity	6
1.3	Microwave heating	6
1.4	Tumor	7
1.5	Sigmoidal modeling of dielectric properties	8
1.6	Distribution of isopotential lines	10
1.7	Resulting image	11
1.8	Voltage deviations	12
2.1	Linear shape functions	17
2.2	Quadratic shape functions	17
2.3	Isoparametric mapping	19
2.4	Gauss quadrature	20
2.5	Assembly of shape functions	21
2.6	Local and global numbering	21
2.7	Connectivity matrix	21
2.8	Numerical solver validation	23
2.9	Validation on cube	24
2.10	Numerical solver validation	25
3.1	Difference imaging	28
4.1	Virtual population models	34
4.2	Image segmentation	35
4.3	Human liver	35
4.4	Tessellation with the Delaunay algorithm	36
4.5	Electrodes starting points	37
4.6	Electrodes placement	37
4.7	Tumor-target	39
4.8	Electrical potential distribution	40

4.9	Reconstruction in 2D	41
4.10	Tumor reconstruction	43
4.11	Conductivity on target	44
5.1	Conductivity on surrounding target	47
5.2	End of treatment	48
5.3	3D slice	49
5.4	3D slice	49
5.5	Slices of reconstructed image	50

List of Tables

1.1	Regression coefficients	9
4.1	Average conductivity values in 2D	38
4.2	Average conductivity values	42

1

Motivation

1.1 Mechanisms of tumour cell death

Modern imaging techniques have paved the way for minimally invasive thermal ablation to be considered common practice in the quest for cancer treatment. Thermal ablation of tumours is the local application of extreme temperatures to induce irreversible cell injury and ultimately tumour apoptosis and coagulative necrosis. Current thermoablative technology offers several advantages over surgical resection: most notably, lower morbidity, increased preservation of surrounding tissues, reduced cost and shorter hospitalization times as well as the ability to treat patients who are poor surgical candidates. Although the efficacy and success rate vary substantially among different tumor types, the outcome relies on efficient monitoring of the biological tissues during the treatment.

Current most commonly used thermal techniques (Chu and Dupuy, 2014) are radiofrequency ablation (RFA) and microwave ablation (MWA), which are high-temperature-based modalities, and cryoablation, which is a low-temperature-based modality. Newer technologies, but less studied, include high-intensity focused ultrasound (HIFU) and laser ablation, which are conceptually similar to high-temperature-based ablation. HIFU is the only completely non-invasive hyperthermic

modality. It uses multiple ultrasound beams and focuses them on a selected focal area to generate temperatures of up to 60 °C using acoustic energy, which causes coagulative necrosis. Laser ablation generates electromagnetic heating and can be very precise and efficient. However because light is easily scattered and absorbed this modality has limited tissue penetration and affects very small areas.

RFA and MWA, as well as laser ablation and HIFU, cause focal hyperthermic injury to ablated cells, which affects the tumour microenvironment and damages cells at the membrane and subcellular levels. Cellular damage depends on the thermal energy that is applied, the rate of application and the thermal sensitivity of the target tissue. Heat-ablated lesions can be thought of as having three zones (Ahmed et al., 2011): the central zone, which is immediately beyond the application tip and which undergoes ablation-induced coagulative necrosis; a peripheral or transitional zone of sublethal hyperthermia, which mostly occurs from thermal conduction of the central area that is either undergoing apoptosis or recovering from reversible injury; and the surrounding tissue that is unaffected by ablation.

At temperatures of around 40–45 °C, irreversible cell damage occurs only after prolonged exposure (from 30 to 60 minutes). At temperatures of above 60 °C, the time that is required to achieve irreversible damage decreases exponentially. Inactivation of vital enzymes is an initial feature of injury. Above 60 °C, rapid protein denaturation occurs, which is immediately cytotoxic and leads to coagulative necrosis (Nikfarjam, Muralidharan, and Christophi, 2005).

1.1.1 Radiofrequency ablation

RF ablation relies on a complete electrical circuit created through the body to conduct RF current. RF current is able to pass through tissue because of the abundance of ionic fluid present; however, tissue is not a perfect conductor and RF current causes resistive heating. Direct RF heating occurs within several millimeters of the electrode. The rest of the final ablation zone is created when thermal conduction pushes heat into the peripheral zone around the electrode. RF current can be applied using “monopolar” or “bipolar” modes. In monopolar mode, a single interstitial electrode (or group of electrodes) is used to deliver current at the tumor site, while surface electrodes (ground pads) complete the electrical circuit through the body. In bipolar mode, current flows between two interstitial electrodes.

In the central zone temperatures between 60 °C and 100 °C are generated by a high-frequency alternating current, which induces frictional heating when the ions in the tissue attempt to follow the changing directions of the alternating current.

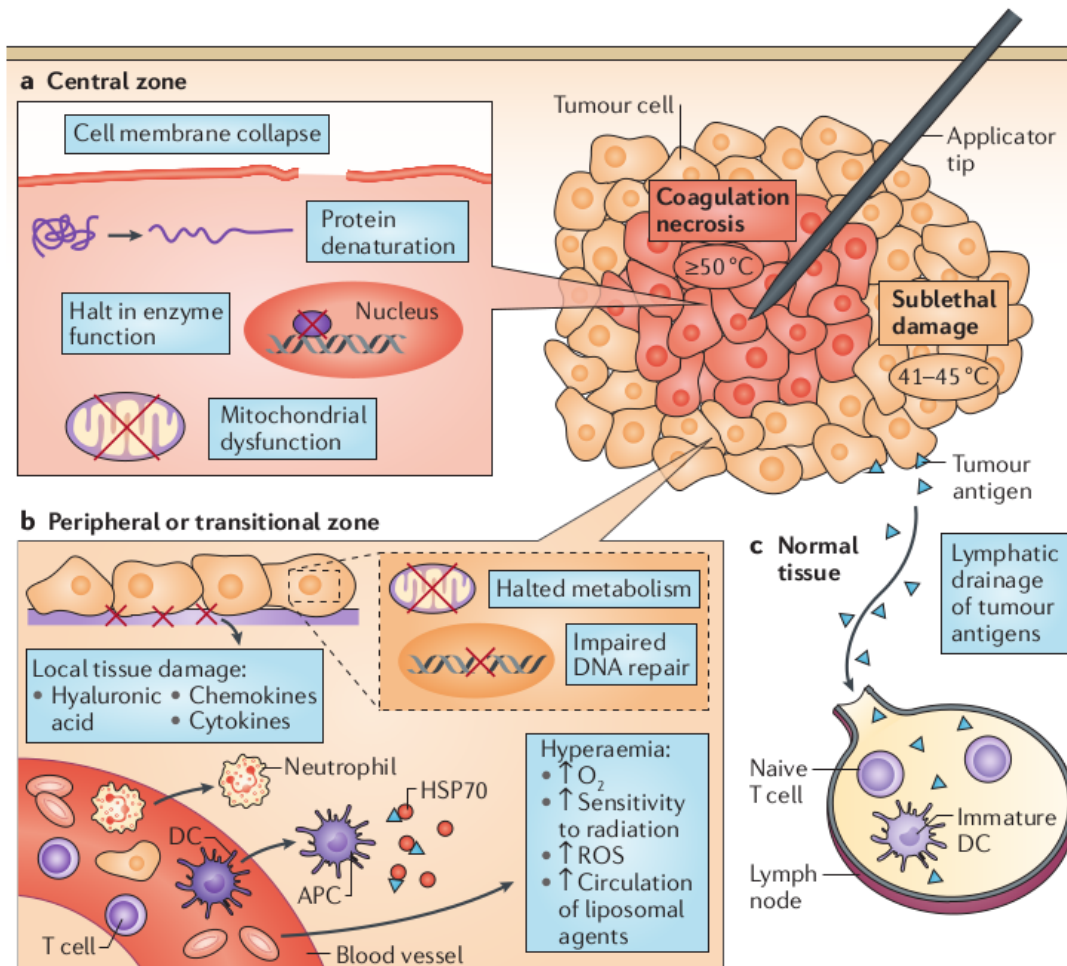


Figure 1.1: The applicator tip is surrounded by three zones. The central zone undergoes coagulative necrosis at temperatures $\geq 50^\circ\text{C}$. The peripheral or transitional zone has a steep negative temperature-gradient. At temperatures between 41°C and 45°C there is still heat-induced injury, but it is sublethal and reversible. Metabolic functions might be deranged or halted, and cells in this zone are vulnerable to further injury; for example, radiation-induced inhibition of DNA repair and cell recovery can eliminate already susceptible cells. (Chu and Dupuy, 2014)

This frictional heating (also known as ‘resistive’ heating) causes cell injury by the above-stated hyperthermic mechanisms and subsequent coagulative necrosis. Interestingly, temperatures >100 °C are less effective, as the desiccation that results at these temperatures, which manifests as water vapour and burnt tissue, increases the tissue impedance and therefore limits further electrical conduction through the remaining tissue.

Additionally, cytotoxic temperatures are difficult to maintain if the ablated tumour is near large blood vessels. This heat-sink effect is a commonly described limitation of RFA and occurs when heat that is absorbed by flowing blood or air is carried away from the area of ablation, thereby dissipating the hyperthermia and decreasing RFA efficacy; because of this, tumour tissue that is adjacent to vasculature is less susceptible to thermal damage (Chu and Dupuy, 2014).

1.1.2 Microwave ablation

During MW ablation an electromagnetic field, which is typically between 900–2500 MHz, is created through an intratumourally placed antenna. This field forces the polar molecules with intrinsic dipoles — predominantly water — within the tissue to continuously realign with the oscillating electric field (figure 1.2). This phenomenon is known as dielectric hysteresis, or rotating dipoles (Lubner et al., 2010). The rotation of the molecules increases their kinetic energy, thereby elevating the temperature of the tissue. In contrast to RFA, MWA does not rely on electric currents and conduction through tissue, so temperatures >100 °C are usually administered without the concern that desiccation will disrupt therapeutic delivery. MWA is therefore more suitable for tissues with higher impedance, including lung and bone, and for tissues with a high water content, such as solid organs and tumours.

MWA has several advantages over RFA. Firstly, since as a principle it does not rely on conduction currents through the tissue but rather on polarization currents, it is not affected by the evaporation of water molecules at very high temperatures, and thus, the therapeutic delivery is not disrupted. Furthermore, it has the ability to achieve better heating of larger tumour volumes and a lower susceptibility to heat-sink effects because microwave systems are faster and more efficient. During RFA, the zone of active heating is limited to a few millimetres around the active electrode, and the remainder of the treated tissue is heated by thermal conduction. By contrast, MWA at certain frequencies can heat tissue up to 2 cm away from the antenna. Another advantage of MWA is the ability to use multiple antennas to

amplify the ablative effect, which enables larger or multi-focal tumours to be ablated simultaneously. Phasing the electromagnetic waves constructively, the heat generated is proportional to the square of the number of antennas; therefore simultaneous activation of multiple antennas results in a synergistic (rather than additive) increase in lesion size (Wright, Lee, and Mahvi, 2003).

However, MWA systems are more cumbersome than RFA and use larger cables. In addition, the antenna is prone to overheating, which necessitates a cooling mechanism to protect the superficial structures along the antenna (Lubner et al., 2010).

1.1.3 Dielectric properties during MWA treatment

The interaction of the EM field radiated by the interstitial antenna with the surrounding tissue is determined by the tissue's dielectric properties. However, heating influences the dielectric properties of the tissue under treatment causing irreversible structural changes principally related to tissue dehydration when temperature rises over about 60 °C. In particular, in a temperature range of 60–80 °C protein denaturation occurs, whereas water vaporization starts as temperature approaches 100 °C.

Information on the dielectric properties of the target tissue plays an important role in determining the radiation efficiency and the specific absorption rate (SAR, W/kg^{-1}) pattern of a MW ablation antenna. In (Lopresto et al., 2012), the authors performed an experimental characterization of the ex vivo dielectric properties of adult bovine liver at 2.45 GHz (a typical frequency for several devices used in MW thermal therapy) during a MTA treatment.

In general, relative permittivity can be expressed as

$$\epsilon_r^* = \epsilon_r - i \frac{\sigma}{\omega \epsilon_0} \quad (1.1)$$

where ϵ_0 is the vacuum permittivity ($\epsilon_0 \approx 8.85 \times 10^{-12} F/m$), $\omega = 2\pi f$, with f representing the frequency (2.45GHz), ϵ_r is the real relative permittivity (dielectric constant) and $\sigma(S/m)$ is the electric conductivity. Electrical permittivity and electrical conductivity were characterized as a function of temperature up to 95 °C (figure 1.4).

The measurements indicate a decrease of both permittivity and conductivity in liver tissue during the ablation as the temperature increases over 60 °C. Once the temperature rises over 90 °C, both drop dramatically and continue to decrease with

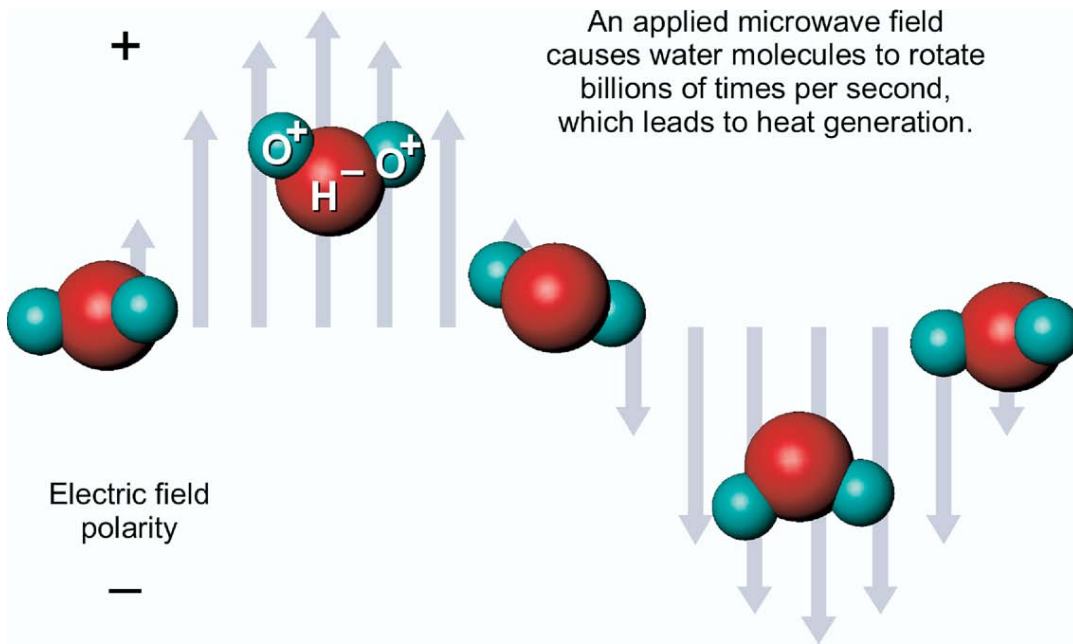


Figure 1.2: Alternating electromagnetic field causes polar molecules to continuous realign, producing kinetic energy and in turn, heat. (Brace, 2009)

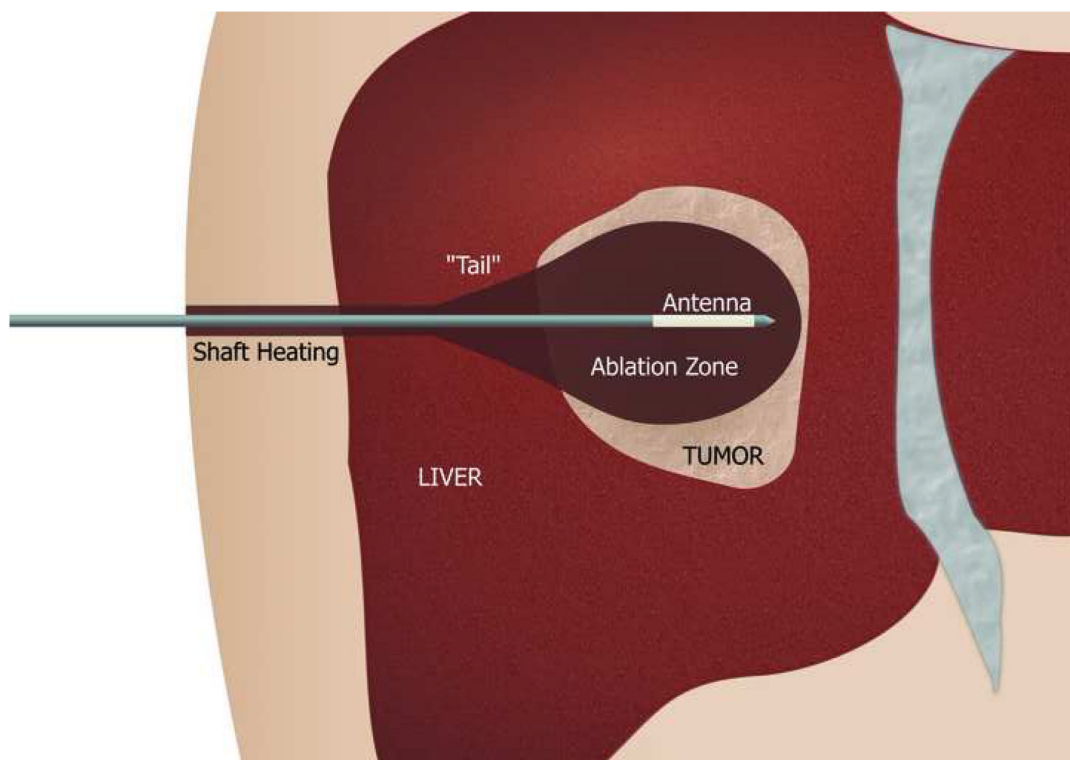
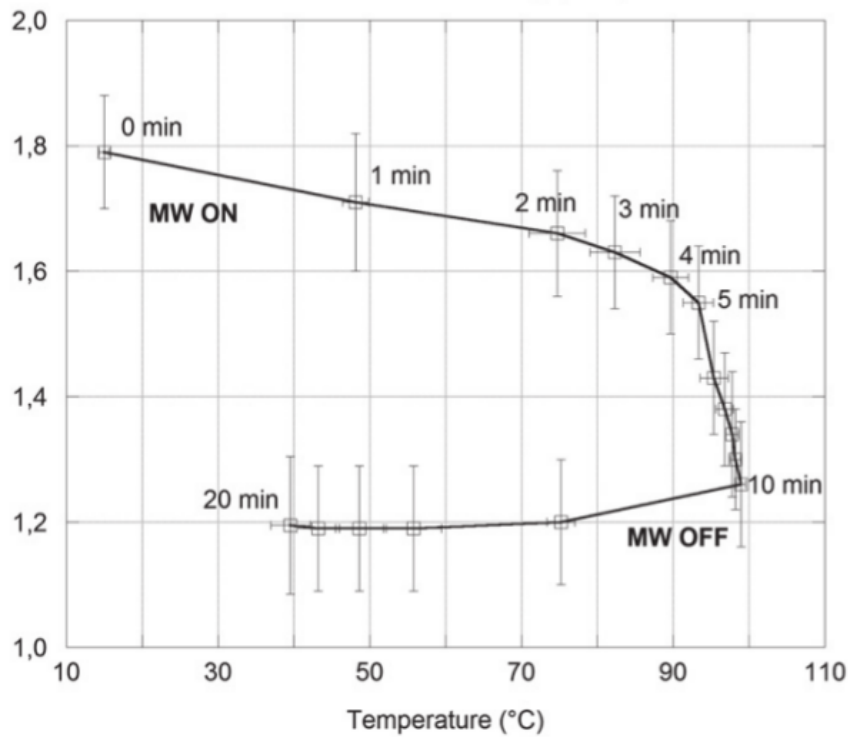
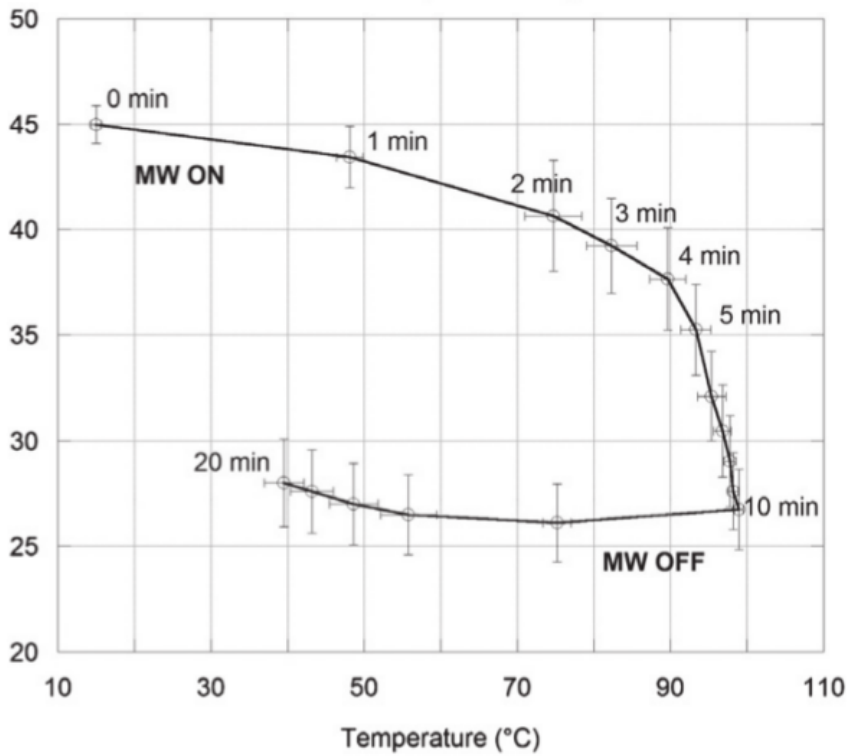


Figure 1.3: Since significant shaft heating that can occur with microwaves, a robust shaft cooling mechanism is required to minimize thermal damage to the subcutaneous tissues and the skin, especially with the development of higher power systems. (Lubner et al., 2010)



(a)



(b)

Figure 1.4: Relative permittivity and electric conductivity as a function of the temperature, measured at 2.45GHz in ex vivo bovine liver during the MTA treatment (30W for 10min) (Lopresto et al., 2012)

exposure time. After switching off the MW field, the values of the dielectric properties remain significantly lower (about 38% for the relative permittivity, and about 33% for the electric conductivity) than the initial ones, evidencing that the measured changes are irreversible.

1.1.4 Regression modeling for dielectric properties in MWA

In (Ji and Brace, 2011) *ex vivo* measurements of dielectric properties during microwave ablation were taken for temperatures that exceeded 100 °C. Furthermore, several regression models for both permittivity and conductivity were investigated. Their results are presented in figure 1.5.

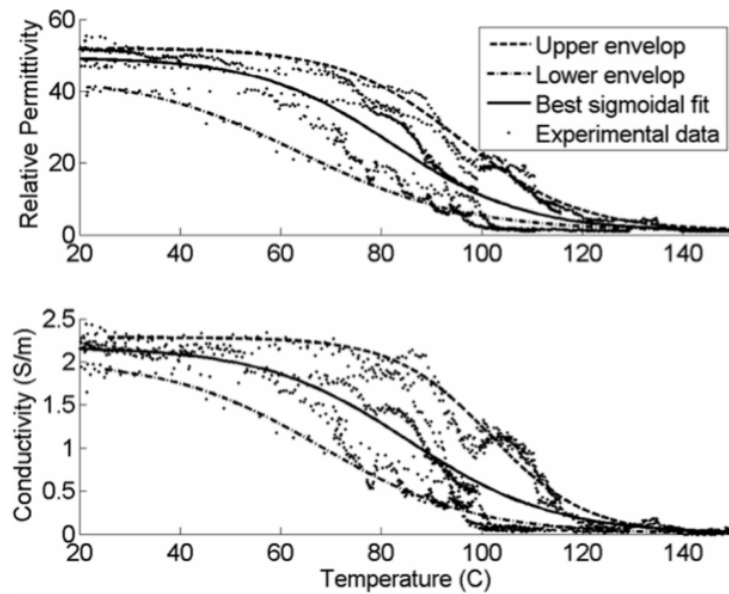


Figure 1.5: Experimental results (dots) of relative permittivity and conductivity versus temperature during microwave ablation. Also shown are the best-fit sigmoidal curves (solid lines), along with the upper and lower envelopes (dashed lines). (Ji and Brace, 2011)

The sigmoidal model which best fitted the behavior of both relative permittivity and conductivity was

$$\epsilon_r(T) = a_3 \left\{ 1 - \frac{1}{1 + e^{a_1(a_2 - T)}} \right\} + 1 \quad (1.2)$$

$$\sigma(T) = a_3 \left\{ 1 - \frac{1}{1 + e^{a_1(a_2 - T)}} \right\} + 1 \quad (1.3)$$

where temperature T is the lone independent variable ($^{\circ}\text{C}$) and a_i ($i = 1, 2, 3$) are the regression coefficients presented in table 1.1.

	a_1	a_2	a_3	a_4
ϵ_r	0.0764	82.271	48.391	0.857
σ	0.0697	85.375	2.173	0.7881

Table 1.1: Regression coefficients for models 1.2 and 1.3 (Ji and Brace, 2011).

Only the sigmoidal model predicted the rapid increase in microwave heating when temperatures exceeded 100°C . However, in contrast to the rapid temperature elevations indicative of direct microwave heating near the antenna, temperatures increased more slowly and linearly farther from the antenna.

1.2 Imaging techniques

To improve the success rate without any adverse effects and reduce recurrence rate after ablation treatments, the therapy requires a non-invasive real-time temperature distribution monitoring method in the treated region during the ablation (Irina, Kirill, and Rinat, 2005). Additionally, the evaluation of the ablated lesion is one of the most important topics related to predicting local recurrence after ablation. For these reasons, often impedance feedback or internal probe temperature is used. However, thermal conduction is affected by dynamic tissue characteristics and the structure of surrounding tissues, such as the vascularity close to the ablated region and its blood flow. Therefore, it is optimal to provide detailed dynamic information to feedback control algorithms. Real-time temperature mapping may assist control of the ablation outcome to protect against coagulation necrosis, over-heating, and associated effects in surrounding tissue.

Well established imaging techniques including ultrasound, Computed Tomography (CT), and Magnetic Resonance Imaging (MRI) have been used for planning, targeting, monitoring, controlling, and assessing treatment response during ablation procedures. MRI using the proton resonance frequency technique can provide highly sensitive temperature distribution information in vivo with high spatial resolution. However, it is difficult to assess ablation outcome in real-time and requires Magnetic Resonance (MR) compatible ablation methods. High intensity focused ultrasound ablation is of interest since ultrasound could be a combined method for treatment and monitoring. However, it requires a skilled operator to treat localized cancer with well-demarcated margins and prior information related to tissue distribution.

Electrical conductivity of a biological tissue reflects ion mobility in intra- and extra-cellular fluids corresponding to temperature, composition of moving ions, cellular morphology of tissue, and other factors. During the last three decades, there have been numerous studies to visualize the conductivity distribution inside the human body (Wi et al., 2015).

1.2.1 Electrical Impedance Tomography

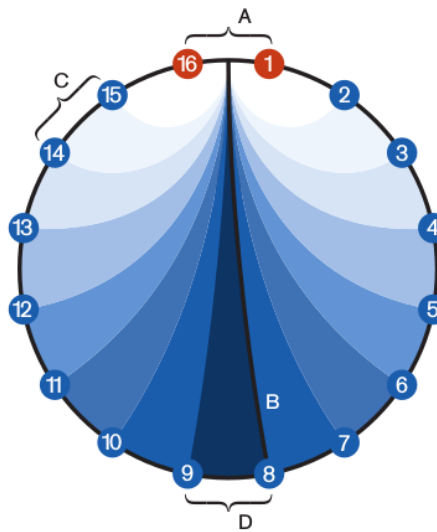


Figure 1.6: Distribution of isopotential lines. (Teschner, Imhoff, and Leonhardt, 2011)

Electrical impedance tomography (EIT) is a technique to provide cross-sectional conductivity images from boundary measurements of voltages subject to externally injected currents (Webster, 1990; Holder, 2005). It has been applied in a number of areas with highest adoption in lung ventilation monitoring due to its high temporal resolution and suitability for bedside monitoring. Typically, conducting surface electrodes are attached to the skin around the body part being examined. Small alternating currents will be applied to some or all of the electrodes, the resulting equi-potentials being recorded from the other electrodes (figures 1.6 1.8). This process will then be repeated for numerous different electrode configurations and finally result in a two-dimensional tomogram according to the image reconstruction algorithms incorporated (figure 1.7).

Mathematically, the problem of recovering conductivity from surface measurements of current and potential is a non-linear inverse problem and is severely ill-posed. The mathematical formulation of the problem is due to Alberto Calderón, and in the mathematical literature of inverse problems it is often referred to as

"Calderón's inverse problem". There is extensive mathematical research on the problem of uniqueness of solution and numerical algorithms for solving it.

Conductivity spectrum can be used as a biomarker to differentiate cancerous tissue from normal because tissue associated with malignant lesions displays a large change in conductivity spectrum caused by differences in cell density, size, and vascularization. Tissue changes occur in ablated tissue and, hence, conductivity imaging has been proposed as a method to monitor temperature distribution and assess the ablated lesion due to ablation (Wi et al., 2015).

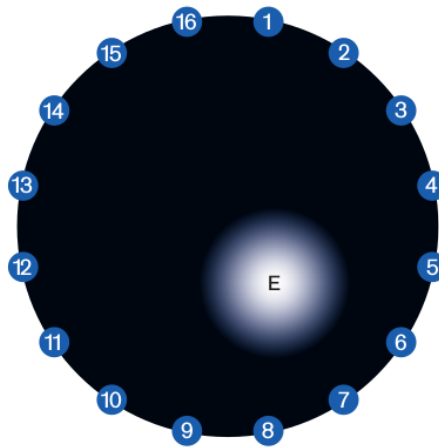


Figure 1.7: Resulting image after successive superposition of all voltage deviations. (Teschner, Imhoff, and Leonhardt, 2011)

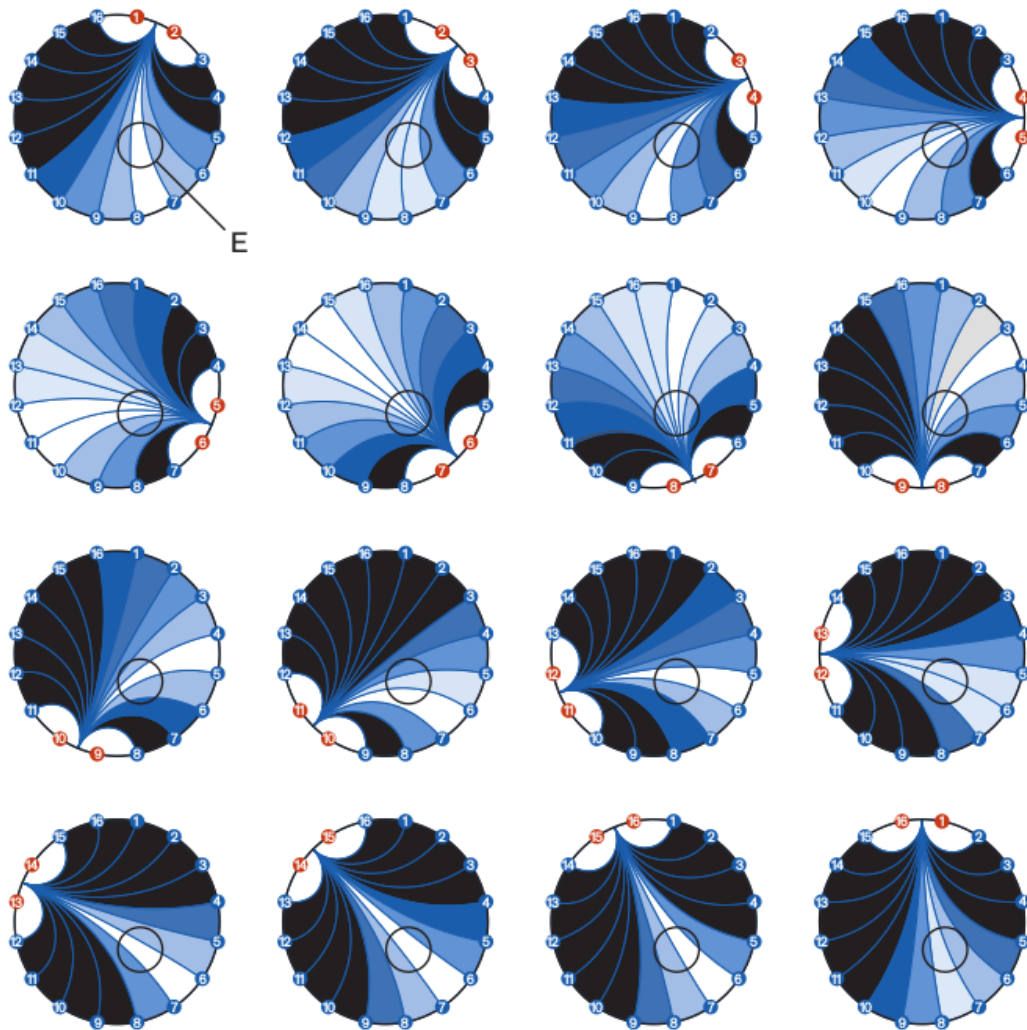


Figure 1.8: Voltage deviations in the presence of a regional increase of impedance. (Teschner, Imhoff, and Leonhardt, 2011)

2

The finite element method

2.1 The static electrical field

The diffusion of the potential in a static electrical field can be calculated by solving the Laplace equation:

$$\nabla^2 u = 0 \quad (2.1)$$

In a general case where particles, energy, or other physical quantities are transferred inside a physical system due to diffusion and convection the *convection-diffusion equation* has to be considered:

$$\frac{\partial u}{\partial t} = \nabla \cdot \sigma \nabla u - \mathbf{v} \nabla u + f \quad (2.2)$$

where σ is the diffusivity in the medium, \mathbf{v} is the average velocity that the quantity is moving with (convection) and f describes the source of the quantity. Should the convection term and the source be absent, the equation truncates to the famous Laplace equation.

The Laplace equation is the simplest elliptic partial differential equation and the finite element method is an excellent way to solve it numerically. A solution u satisfying 2.1 will also satisfy boundary conditions on the boundary $\partial\Omega$ of Ω :

$$u = g_D \quad \text{on } \partial\Omega_D \quad (2.3)$$

$$\frac{\partial u}{\partial n} = g_N \quad \text{on } \partial\Omega_N \quad (2.4)$$

where $\frac{\partial u}{\partial n}$ denotes the directional derivative in the direction normal to the boundary (conventionally pointing outwards). On the $\partial\Omega_D$ the boundary condition is of Dirichlet type, whereas on the $\partial\Omega_N$ we have Neumann boundary condition.

2.1.1 Weak formulation

A sufficiently smooth function u satisfying 2.1 and both 2.3 and 2.4 conditions is known as a classical solution to the boundary value problem. For a Dirichlet problem, u is a classical solution only if it has continuous second derivatives in Ω and is continuous up to the boundary. Since we demand the solution in any non-smooth domain an alternative description of the boundary problem is required. Since this alternative description is less restrictive it is called a weak formulation.

To derive a weak formulation of a Laplace problem we require that for an appropriate set of *test functions* v

$$\int_{\Omega} (\nabla^2 u) v = 0 \quad (2.5)$$

This formulation exists provided that the integrals are well defined. If u is a classical solution then it must also satisfy 2.5. If v is sufficiently smooth however, then the smoothness required of u can be reduced by using the derivative of a product rule and the divergence theorem

$$\begin{aligned} \int \nabla \cdot (v \nabla u) &= \int \nabla v \cdot \nabla u + \int v \nabla^2 u \\ - \int v \nabla^2 u &= \int \nabla v \cdot \nabla u - \int_{\partial\Omega} v \frac{\partial u}{\partial n} \end{aligned}$$

so that

$$\int \nabla v \cdot \nabla u = \int_{\partial\Omega} v \frac{\partial u}{\partial n} \quad (2.6)$$

In case of Dirichlet conditions, the value of the solution is exactly known, $u = g_D$, and hence test functions are not defined on the boundary, $v = 0$. This is in contrast to the Neumann case where the solution and the test functions are not restricted on the boundary. Taking 2.4 into account, 2.6 becomes

$$\int \nabla v \cdot \nabla u = \int_{\partial\Omega_N} v g_N \quad \text{for all suitable } v \quad (2.7)$$

All suitable v functions are those whose derivative is square-integrable (Elman, Silvester, and Wathen, 2005). In contrast, a classical solution of a Laplace problem has to be twice differentiable in Ω , which is a much more stringent requirement than the square integrability of first derivatives. Using 2.7 instead as the starting point enables us to look for approximate solutions that only need satisfy the smoothness requirement and the essential boundary conditions.

2.1.2 The Galerkin approximation

We construct an approximation method by assuming for the solution of the 2.7 a finite n -dimensional vector space of test functions for which $\{\phi_1, \phi_2, \dots, \phi_n\}$ is a convenient basis. In that sense, the finite element approximation for the solution u_h is uniquely associated with the vector $\mathbf{u} = (\mathbf{u}_1, \mathbf{u}_2, \dots, \mathbf{u}_n)^T$ of real coefficients in the expansion

$$u_h = \sum_{j=1}^n \mathbf{u}_j \phi_j \quad (2.8)$$

The functions $\phi_i, i = 1, \dots, n$ in 2.8 define a set of trial functions. In the finite element context they are called shape functions. The Galerkin approximation (or more precisely *Bubnov-Galerkin*, contrary to the *Petrof-Galerkin*), indicates that the choice of the trial functions coincides with the test functions $\phi \equiv v$ (Elman, Silvester, and Wathen, 2005).

The result of the Galerkin approximation is a finite-dimensional version of the weak formulation:

$$\int_{\Omega} \nabla u_b \cdot \nabla v_b = \int_{\partial\Omega_N} v_b g_N \quad \text{for all } v_b \quad (2.9)$$

Substituting 2.8 into 2.9 yields

$$\sum_{j=1}^n \mathbf{u}_j \int_{\Omega} \nabla \phi_j \cdot \nabla \phi_i = \int_{\partial\Omega_N} \phi_i g_N \quad (2.10)$$

for $i = 1, \dots, n$. This can be written in matrix form as a linear system of equations

$$\mathbf{A}\mathbf{u} = \mathbf{b} \quad (2.11)$$

with

$$A = [a_{ij}], \quad a_{ij} = \int_{\Omega} \nabla \phi_j \cdot \nabla \phi_i \quad (2.12)$$

and

$$b = [b_i], \quad b_i = \int_{\partial\Omega_N} \phi_i g_N \quad (2.13)$$

The matrix A is referred to as the *stiffness matrix*. The stiffness matrix (2.12) is symmetric and is also positive-definite (Elman, Silvester, and Wathen, 2005), and thus, its linear system can be solved with fast iterative methods.

2.2 Implementation

The first step over implementing the finite element method is to generate a mesh of elements consisting of tetrahedra over the three dimensional physical domain, or triangles in a two dimensional plane. A very efficient algorithm to perform such a procedure is the Delaunay triangulation and is implemented in the CGAL library (The CGAL Project, 2016). After obtaining a tetrahedral mesh, the construction of the Galerkin system follows. Essential conditions are imposed after the assembly of the element contributions into the Galerkin system has been completed. Finally, we obtain the solution of the discrete system using a linear solver that exploits the sparsity of the coefficient matrix.

2.2.1 Shape functions

The points where triangle vertices meet are called nodes. For each node, we define ϕ_j to be a linear function (i.e. of the form $a + bx + cy + dz$) on each tetrahedral element satisfying the interpolation condition

$$\phi(\text{node } i) = \begin{cases} 1 & \text{when } i = j \\ 0 & \text{when } i \neq j \end{cases} \quad (2.14)$$

There are precisely four basis functions that are nonzero on any particular tetrahedral element, corresponding to the four coefficients needed to define the linear approximation in the element. Higher order tetrahedral elements can be defined by introducing additional nodes.

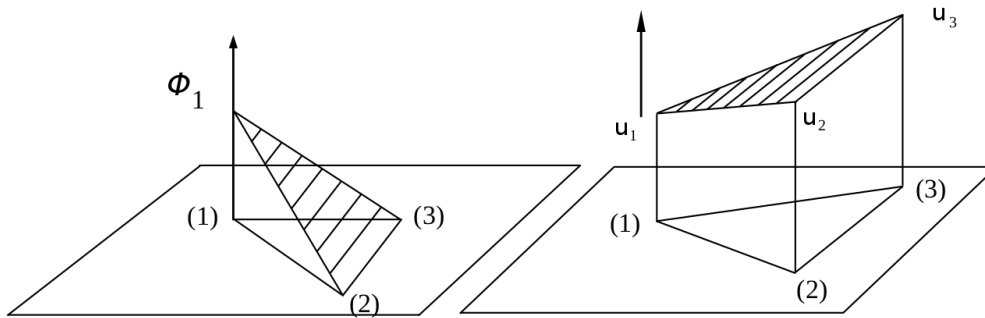


Figure 2.1: Linear shape function of node (1) and linear approximation of solution

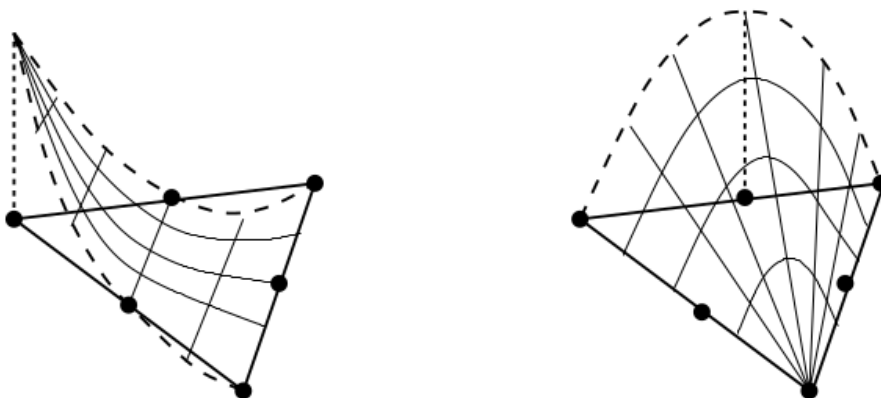


Figure 2.2: Quadratic shape functions

The key idea in the implementation of finite element methodology is to consider everything "elementwise", that is, locally one element at a time. The stiffness matrix from 2.10 can be written as

$$\sum_{j=1}^n \mathbf{u}_j \int_{\Omega} \nabla \phi_j \cdot \nabla \phi_i = \sum_{j=1}^n \mathbf{u}_j \left\{ \sum_{\Delta_k} \int_{\Delta_k} \nabla \phi_j \cdot \nabla \phi_i \right\} \quad (2.15)$$

where Δ_k is an element of the triangulation. When forming the sum over the elements in 2.15 we need only to take account of those elements where the basis functions ϕ_i and ϕ_j are both nonzero. This means that entries a_{ij} and b_i in the Galerkin system can be computed by calculating contributions from each element, and then gathering them together (assembly).

For an element k with n_k degrees of freedom, there are exactly n_k shape functions. As such, the solution within the elements takes the form

$$u_b|_k = \sum_{i=1}^{n_k} \mathbf{u}_i^{(k)} \psi_{k,i} \quad (2.16)$$

assuming that

$$\{\psi_{k,1}, \psi_{k,2}, \dots, \psi_{k,n_k}\} \quad (2.17)$$

are the local shape functions. Thus, for each element we need to compute $n_k \times n_k$ matrices A_k and n_k sized vectors b_k such that

$$a_{ij} = \int_{\Delta_k} \nabla \psi_{k,i} \cdot \nabla \psi_{k,j} \quad (2.18)$$

$$b_i = \int_{\partial\Omega} \psi_i g_N \quad (2.19)$$

The matrix A_k is referred to as the *element stiffness matrix* associated with element Δ_k

2.2.2 Jacobian transformation

The first stage in the computation of the element stiffness matrix A_k is to map from a reference element Δ_* onto the given element Δ_k , as illustrated in figure 2.3. The mapping is defined for all points $(x, y) \in \Delta_k$ and for a triangle element is given by

$$x(\xi, \eta) = x_1 N_1(\xi, \eta) + x_2 N_2(\xi, \eta) + x_3 N_3(\xi, \eta) \quad (2.20)$$

$$y(\xi, \eta) = y_1 N_1(\xi, \eta) + y_2 N_2(\xi, \eta) + y_3 N_3(\xi, \eta) \quad (2.21)$$

where

$$\begin{aligned} N_1(\xi, \eta) &= 1 - \xi - \eta \\ N_2(\xi, \eta) &= \xi \\ N_3(\xi, \eta) &= \eta \end{aligned} \quad (2.22)$$

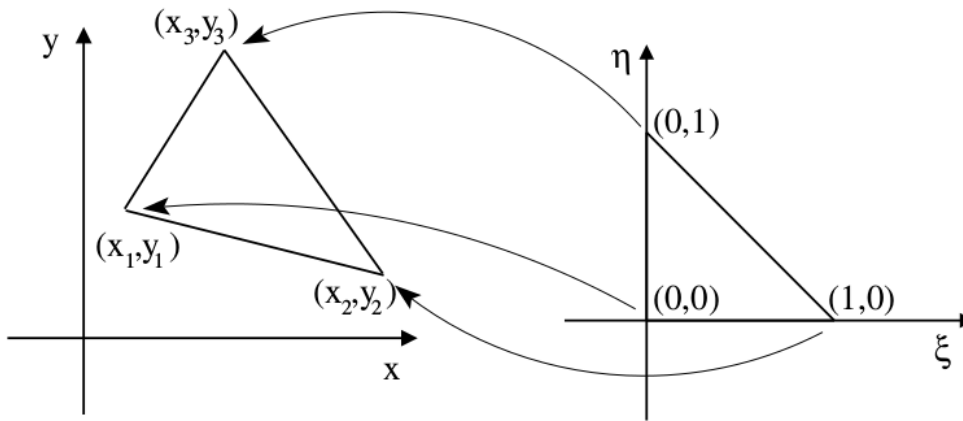


Figure 2.3: Isoparametric mapping of reference element

are the shape functions defined on the reference element. Clearly the map from the reference element onto Δ_k is differentiable, thus, for a function $\phi(\xi, \eta)$ we can transform derivatives via the *Jacobian matrix*

$$\begin{bmatrix} \frac{\partial \phi}{\partial \xi} \\ \frac{\partial \phi}{\partial \eta} \end{bmatrix} = \begin{bmatrix} \frac{\partial x}{\partial \xi} & \frac{\partial y}{\partial \xi} \\ \frac{\partial x}{\partial \eta} & \frac{\partial y}{\partial \eta} \end{bmatrix} \begin{bmatrix} \frac{\partial \phi}{\partial x} \\ \frac{\partial \phi}{\partial y} \end{bmatrix} \quad (2.23)$$

The fact that $|J_k(\xi, \eta)| \neq 0$ for all points $(\xi, \eta) \in \Delta_*$ is very important; it ensures that the inverse mapping from Δ_k onto the reference element is uniquely defined and is differentiable. As such, the derivative transformation for a triangle can be inverted to produce

$$\begin{bmatrix} \frac{\partial \phi}{\partial x} \\ \frac{\partial \phi}{\partial y} \end{bmatrix} = \begin{bmatrix} \frac{\partial \xi}{\partial x} & \frac{\partial \eta}{\partial x} \\ \frac{\partial \xi}{\partial y} & \frac{\partial \eta}{\partial y} \end{bmatrix} \begin{bmatrix} \frac{\partial \phi}{\partial \xi} \\ \frac{\partial \phi}{\partial \eta} \end{bmatrix} \quad (2.24)$$

Using 2.24 we can compute the derivatives of the shape functions of the reference element with respect to the axis of the k element and plug them in to easily compute each element of the local stiffness matrix:

$$a_{ij}^{(k)} = \int_{\Delta_k} \frac{\partial \psi_{k,i}}{\partial x} \frac{\partial \psi_{k,j}}{\partial x} + \frac{\partial \psi_{k,i}}{\partial y} \frac{\partial \psi_{k,j}}{\partial y} dx dy \quad i, j = 1, \dots, n_k \quad (2.25)$$

$$= \int_{\Delta_*} \left\{ \frac{\partial \psi_{*,i}}{\partial \xi} \frac{\partial \psi_{*,j}}{\partial \xi} + \frac{\partial \psi_{*,i}}{\partial \eta} \frac{\partial \psi_{*,j}}{\partial \eta} \right\} |J_k| d\xi d\eta \quad (2.26)$$

The last step to calculating the stiffness functions is to compute the integrals. We use the multi-dimensional Gauss quadrature for this. The integral is approximated by the summation

$$a_{ij}^{(k)} = \sum_{s=1}^m \sum_{t=1}^m w_{st} |J_k(\xi_s, \eta_t)| \left\{ \frac{\partial \psi_{*,i}}{\partial \xi} \frac{\partial \psi_{*,j}}{\partial \xi} + \frac{\partial \psi_{*,i}}{\partial \eta} \frac{\partial \psi_{*,j}}{\partial \eta} \right\} \Big|_{\xi_s, \eta_t} \quad (2.27)$$

where the quadrature points (ξ_s, η_t) correspond to the associated weights w_{st} for each integration rule (Hughes, 1987).

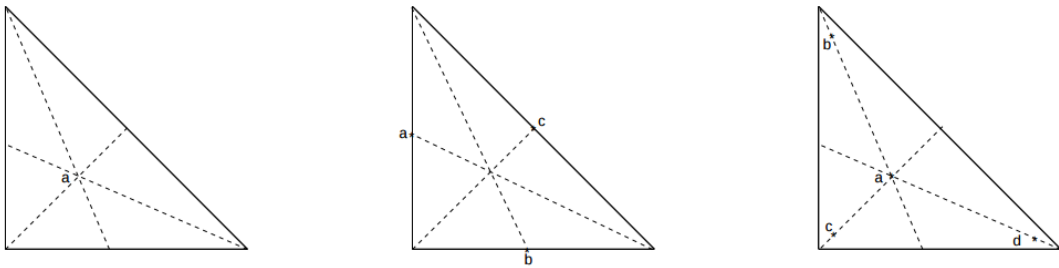


Figure 2.4: Gauss quadrature rule on the reference element

2.2.3 Assembly

The assembly process is implemented by calculating the stiffness matrix for every element. Then the contribution of each element to the corresponding node is added

to the global matrix of coefficients.

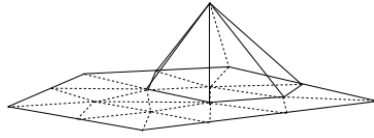


Figure 2.5: Assembly of shape functions around each node.

The main computational issue is the need for careful bookkeeping to ensure that the element contributions are added into the correct locations in the coefficient matrix A and the vector b . The simplest way of implementing the process is to represent the mapping between local and global entities using a connectivity matrix. This process is illustrated in figures 2.6 and 2.7.

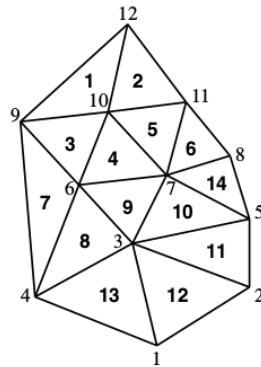


Figure 2.6: Local and global numbering for a triangular mesh.

1	2	3	4	5	6	7	8	9	10	11	12	13	14
9	12	9	6	10	11	4	4	6	5	5	2	1	8
10	10	6	7	7	7	6	3	3	7	3	3	3	7
12	11	10	10	11	8	9	6	7	3	2	1	4	5

Figure 2.7: Connectivity matrix of global indices to local element nodes

As a last important step after the assembly has been completed, boundary conditions must be imposed. Dirichlet boundary conditions are imposed after the assembly and Neumann boundary conditions are imposed last, after the Dirichlet conditions. There are several approaches to imposing the Dirichlet conditions but the one used for this study was to modify the row and column of the Galerkin matrix corresponding to the boundary node so that the diagonal value is unity and the off-diagonal entries are set to zero. Furthermore, the corresponding value of the

b vector is set to the boundary value. For the Neumann conditions, they are imposed by running through the boundary edges and evaluating edge contributions using one-dimensional Gauss quadrature.

2.3 Solution of discrete system

The coefficient matrix of the linear system arising from finite element discretization of the Poisson equation is symmetric positive-definite. Following the Galerkin approximation discussed in this chapter, is also sparse. That is, only a very small proportion of its entries is nonzero. For this study a *Krylov subspace* method was applied to produce the solution for the static field, and in particular the **conjugate gradient method** with **Jacobi preconditioner**. Open source numerical library PetSc was used (Balay et al., 2016).

For the iterative solution of the linear system it would be ideal if the number of iterations required to satisfy the stopping criterion did not grow under mesh refinement, so that the computational work would grow linearly with the dimension of the discrete system. *Preconditioning* is usually employed in order to achieve this ideal or to get closer to it. The basic idea is to construct a matrix (or a linear process), P say, that approximates the coefficient matrix A but for which it requires little work to apply the action of the inverse of P , that is, to compute $P^{-1}v$ for given v . One may then think of solving

$$P^{-1}A\mathbf{u} = P^{-1}b \quad (2.28)$$

instead of $A\mathbf{u} = b$; they clearly have the same solution. If P is a good approximation of A , then it might be expected that the conjugate gradient iteration will be more rapidly convergent for the preconditioned system 2.28 than for the original system and the overall computational work may be significantly reduced. For very large problems, preconditioning may be necessary to make computation feasible.

The Jacobi preconditioner is one of the simplest forms of preconditioning, in which the preconditioner is chosen to be the diagonal of the matrix

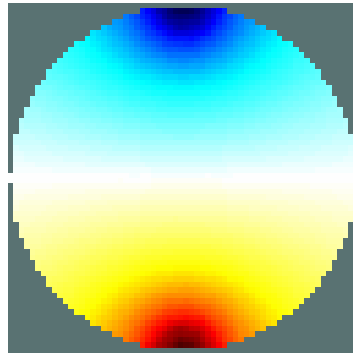
$$P = \text{diag}(A) \quad (2.29)$$

Assuming $A_{ii} \neq 0, \forall i$, we get

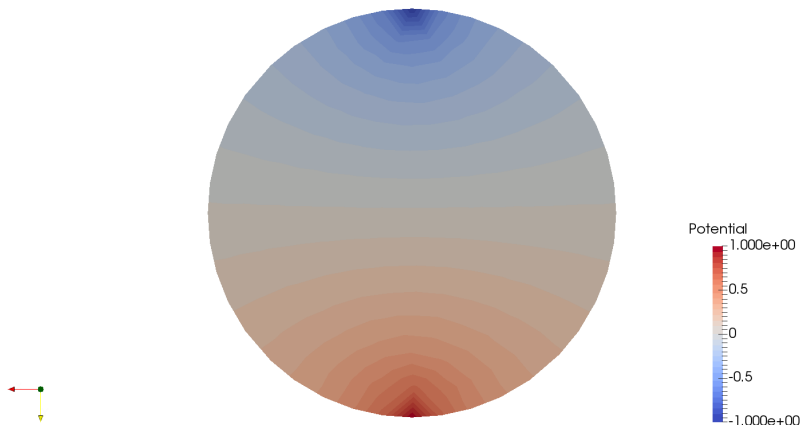
$$P_{ij}^{-1} = \frac{\delta_{ij}}{A_{ij}} \quad (2.30)$$

2.4 Validation

The self-implemented electrostatic numerical solver was validated in two ways. First, it was validated against EIDORS' (Polydorides and Lionheart, 2002; Adler and Lionheart, 2006; Polydorides, 2002) forward solver on a homogeneous cylinder. The result is shown in figure 2.8.



(a) Eiders numerical solution



(b) Finite element solver numerical solution

Figure 2.8: Finite element solver validation against Eiders' forward solver.

Furthermore, it was compared to some analytical solutions. Simple geometries were designed out of which the analytical solution is obvious and can be calculated easily. Two cases are presented here, a cube and a two spheres in figures 2.9 and 2.10

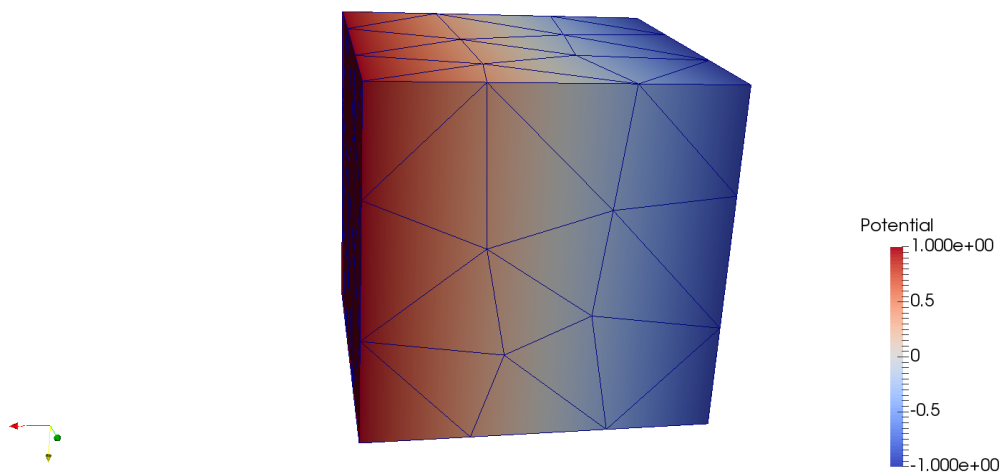
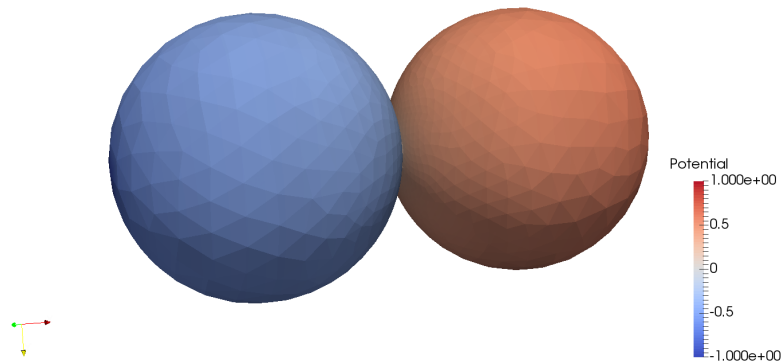
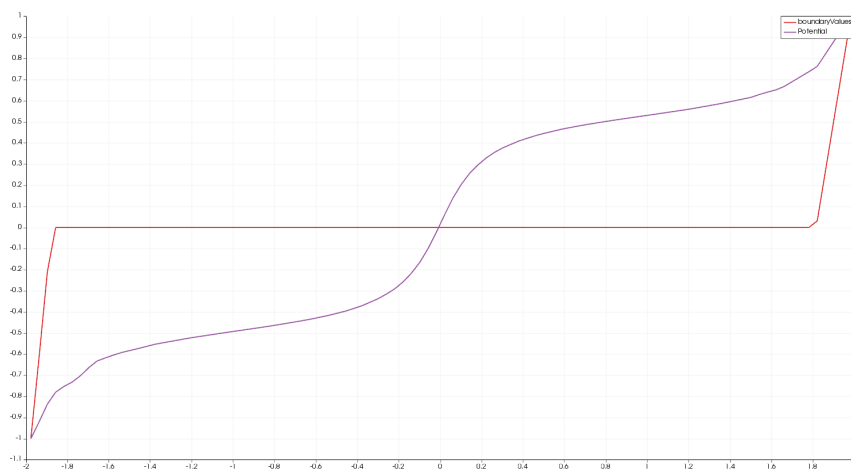


Figure 2.9: Boundary conditions were set at -1 at the left face and +1 at the right face of the cube. Exactly zero is expected in the middle.



(a) Two homogeneous spheres barely touching.



(b) Plot of the potential (with purple) along a line passing through the middle from the very left to the very right. The potential is exactly zero in the middle, as expected. With red color is the initial values of the potential along the same line.

Figure 2.10: Boundary values were set -1 at a few points at the very left of the sphere in the left part of the image, and +1 at the very right part of the right sphere. Potential is diffused through the thin part where they barely touch.

3

Image Reconstruction

3.1 Inverse problem in EIT

The process of estimating the impedance from the measured data is known as the inverse problem in EIT. The inverse problem is solved using a reconstruction algorithm of which there are two primary types in EIT. Static imaging attempts to recover an estimate of the absolute conductivity of the medium from which the boundary data was acquired. Static imaging is discussed in section 3.3. Difference imaging attempts to recover an estimate of the change in conductivity over some interval based on data frames measured at two times, see figure 2.3. Difference images can be calculated in a single step with a linearized algorithm, however this assumes that the impedance change over the interval is small. For large impedance changes one needs to solve the non-linear problem with an iterative algorithm.

Calculation of the impedance or impedance changes based on the boundary voltage data is an instance of an ill-conditioned, inverse problem. Such problems are unstable and require some method of improving the conditioning to achieve stability. The most common method is regularization, which involves trading off fidelity to the data against adherence to some a priori condition on the solution.

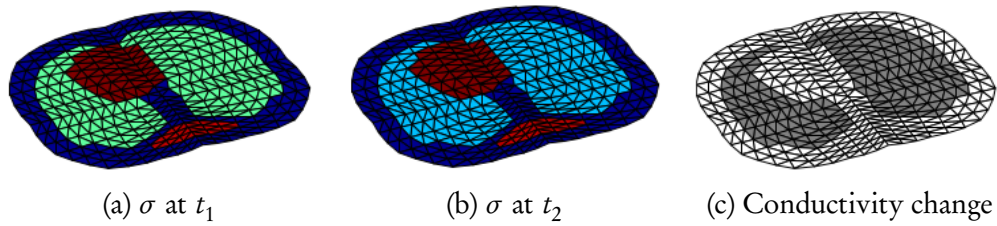


Figure 3.1: Example of difference imaging reconstruction (Graham, 2007)

3.2 Reconstruction algorithm

3.2.1 General statement of the problem

The objective of an inverse problem is to find the best model m such that

$$d = Gm \quad (3.1)$$

where G is an operator describing the explicit relationship between the observed data, d , and the model parameters. In the most general context, G represents the governing equations that relate the model parameters to the observed data (i.e., the governing physics). In the case of a discrete linear inverse problem d and m are vectors, and G is a matrix, often called the observation matrix. In the context of EIT, the observed data correspond to the electric potential and the model parameters consist the electrical conductivity of the biological tissues.

To solve for the model parameters that fit our data we need to invert the matrix G , so that

$$m = G^{-1}d \quad (3.2)$$

However, matrix G is almost never invertible, since it depends on both the independent variable and the parameters.

3.2.2 Non-linear least squares

Because we cannot directly invert the observation matrix, we use methods from non-linear regression analysis. The basis of the method is to approximate the model by a linear one and to refine the parameters by successive iterations.

Considering a set of m data points, $(x_1, y_1), (x_2, y_2), \dots, (x_m, y_m)$ and a model function $f(x, \beta)$ that in addition to the variable x also depends on n parameters $\beta = (\beta_1, \beta_2, \dots, \beta_n)$, with $m \geq n$, it is desired to find vector β of parameters such that the model fits best the data, in the least squares sense. That is, the sum of squares

$$S = \sum_{i=1}^m r_i^2 \quad (3.3)$$

is minimized, where residuals r_i are given by

$$r_i = y_i - f(x_i, \beta) \quad (3.4)$$

for $i = 1, 2, \dots, m$.

The minimum value of S occurs when its gradient is zero. Since the model contains n parameters there are n gradient equations:

$$\frac{\partial S}{\partial \beta_j} = 2 \sum_i r_i \frac{\partial r_i}{\partial \beta_j} = 0 \quad (j = 1, \dots, n) \quad (3.5)$$

In an nonlinear system, the derivatives $\frac{\partial r_i}{\partial \beta_j}$ are functions of both the independent variable and the parameters, so these gradient equations do not have a closed solution. Instead, initial values must be chosen for the parameters. Then, the parameters are refined iteratively, that is, the values are obtained by successive approximation,

$$\beta_j^{k+1} = \beta_j^k + \Delta \beta_j \quad (3.6)$$

where k is an iteration number and the vector of increments, $\Delta \beta$ is known as the shift vector. At each iteration the model is linearized by approximation to a first-order Taylor series expansion about β^k

$$f(x_i, \beta) \approx f(x_i, \beta^k) + \sum_j \frac{\partial f(x_i, \beta^k)}{\partial \beta_j} (\beta_j - \beta_j^k) = f(x_i, \beta^k) + \sum_j J_{ij} \Delta \beta_j \quad (3.7)$$

The Jacobian, J , is a function of constants, the independent variable and the parameters, so it changes from one iteration to the next. Thus, in terms of the linearized model we calculate the residuals and their derivatives

$$\frac{\partial r_i}{\partial \beta_j} = -J_{ij} \quad (3.8)$$

$$r_i = y_i - f(x, \beta) = (y_i - f(x, \beta^k)) + (f(x, \beta^k) - f(x, \beta)) = \Delta y_i - \sum_{s=1}^n J_{is} \Delta \beta_s \quad (3.9)$$

and by substituting 3.8 and 3.9 into 3.5 we get

$$\begin{aligned} -2 \sum_{i=1}^m J_{ij} \left(\Delta y_i - \sum_{s=1}^n J_{is} \Delta \beta_s \right) &= 0 \\ \sum_{i=1}^m \sum_{s=1}^n J_{ij} J_{is} \Delta \beta_s &= \sum_{i=1}^m J_{ij} \Delta y_i \quad (j = 1, \dots, n) \end{aligned}$$

or written in matrix notation

$$(\mathbf{J}^T \mathbf{J}) \Delta \beta = \mathbf{J}^T \Delta \mathbf{y}$$

$$\Delta \beta = (\mathbf{J}^T \mathbf{J})^{-1} \mathbf{J}^T \Delta \mathbf{y} \quad (3.10)$$

The matrix $(\mathbf{J}^T \mathbf{J})^{-1} \mathbf{J}^T$ is the so called *Moore–Penrose pseudoinverse* matrix of J .

3.2.3 Gauss–Newton algorithm

The Gauss–Newton algorithm is a modification of Newton’s method for finding a minimum of a function. The algorithm iteratively finds the value of the variables which minimizes the sum of squares in 3.3. Starting with an initial guess $\beta^{(0)}$ for the minimum, the algorithm proceeds with the iterations

$$\beta^{(k+1)} = \beta^{(k)} - (\mathbf{J}^T \mathbf{J})^{-1} \mathbf{J}^T \mathbf{r}(\beta^{(k)}) \quad (3.11)$$

where the Jacobian matrix is

$$J_{ij} = \frac{\partial r_i(\beta^{(k)})}{\partial \beta_j} \quad (3.12)$$

3.2.4 Tikhonov regularization

A regularization method is defined as an inversion method depending on a single real parameter $\lambda \geq 0$, which yields a family of approximate solutions. Discrete regularization techniques include truncated singular value decomposition, maximum entropy, and a number of generalized least squares schemes including Twomey and Tikhonov regularization methods. All of these methods attempt to reduce the effects of solving an ill-conditioned system by restoring continuity of the solution on the data (Andler and Guardo, 1996).

The most widely referenced regularization method is the Tikhonov method. With Tikhonov regularization additional information about the solution, commonly referred to as prior information, is incorporated into the solution as an additional term in the least squares minimization. In this way, rather than minimizing $(\mathbf{y} - \mathbf{J}\beta)^2$ we minimize the expression

$$\min\{(\mathbf{y} - \mathbf{J}\beta)^2 + \lambda^2(\mathbf{R}\beta)^2\} \quad (3.13)$$

Here R is a regularization matrix that is often diagonal or banded diagonal and the expression $\lambda^2(\mathbf{R}\mathbf{x})^2$ represents some prior information about the conductivity. This is a quadratic minimization that is guaranteed to have a unique solution for $\lambda > 0$. The most often used regularization matrices in EIT are the identity matrix and the classic Tikhonov regularization refers to the case where $\mathbf{R} = \mathbf{I}$. The implied prior assumptions when the classic Tikhonov regularization is used are that x is either small or slowly changing.

The Gauss–Newton method when the Tikhonov regularization is applied becomes

$$\beta^{(k+1)} = \beta^{(k)} - (\mathbf{J}^T \mathbf{J} + \lambda^2 \mathbf{R})^{-1} \mathbf{J}^T r(\beta^{(k)}) \quad (3.14)$$

The parameter λ is called the “regularization parameter” or “hyperparameter” and controls the trade-off between solution stability and nearness of the regularized

solution β to the un-regularized solution $\hat{\beta}$. This can be understood as the approximation error in the absence of measurement noise and the discretization noise due to finite precision arithmetic.

The use of Tikhonov style regularization techniques is equivalent to introducing a priori information to the reconstruction process. The fundamental prior information of the conductivity solution is that it is a positive function. Such methods provide stability but force solutions to be smooth in some sense thus eliminating the possibility of non-smooth solutions.

3.2.5 Noser regularization

The NOSER regularization (Cheney et al., 1990) is proven to produce better results than the Tikhonov regularization for 3D problems where the ill-conditioning is more apparent. Instead of using the identity matrix for the regularization matrix, we use

$$R = \text{diag}(J^T J) \quad (3.15)$$

thus, the NOSER regularized Gauss-Newton method becomes

$$\beta^{(k+1)} = \beta^{(k)} - (J^T J + \lambda^2 \text{diag}(J^T J))^{-1} J^T r(\beta^{(k)}) \quad (3.16)$$

3.2.6 Application in 3D EIT

To apply the Gauss-Newton reconstruction algorithm in difference imaging we define $\hat{x} = \Delta\sigma = \sigma_2 - \sigma_1$ the change in a finite element conductivity distribution due to a change in difference signal, $z = v_2 - v_1$, over a time interval (t_1, t_2) . σ_1 is the background known value of the conductivity. In this sense, the reconstruction method in 3D is written as

$$\hat{x} = (H^T H + \lambda^2 \text{diag}(H^T H))^{-1} H^T z \quad (3.17)$$

where $H = \left. \frac{\partial z_i}{\partial x_j} \right|_{\sigma_1}$ is the Jacobian.

4

Results

In this chapter we present the results of an *in silico* implementation of multiple image reconstructions during microwave ablation treatment using electrical impedance tomography. In place of real measurements that are taken during an actual EIT procedure, we assume decrease of dielectric properties as described in sections 1.1.3 and 1.1.4, and solve the static electrical field to acquire *in silico* measurements of the electric potential. Microwave frequency of 2.45 GHz was assumed.

The finite element method was used as described in chapter 2 to solve the Laplace equation for each pair of electrodes. Open source numerical package EIDORS (Polydorides and Lionheart, 2002; Adler and Lionheart, 2006; Polydorides, 2002) was used to implement image reconstruction following the methods described in chapter 3.

A realistic human model that was based on magnetic resonance imaging was used. A tumor-target inside the human liver and the surrounding electrodes were designed to fit the model simulating a real EIT procedure. Discussion of the results and suggestions for future work follow in the next chapter.

4.1 Human models

4.1.1 Virtual population

The Virtual Population (ViP) models are a set of detailed high-resolution anatomical models created from magnetic resonance image data of volunteers (Gosselin et al., 2014). The images used in this study were acquired with a resolution of $1 \text{ mm} \times 1 \text{ mm} \times 1 \text{ mm}$ and consist of 77 different tissues for the adult models.

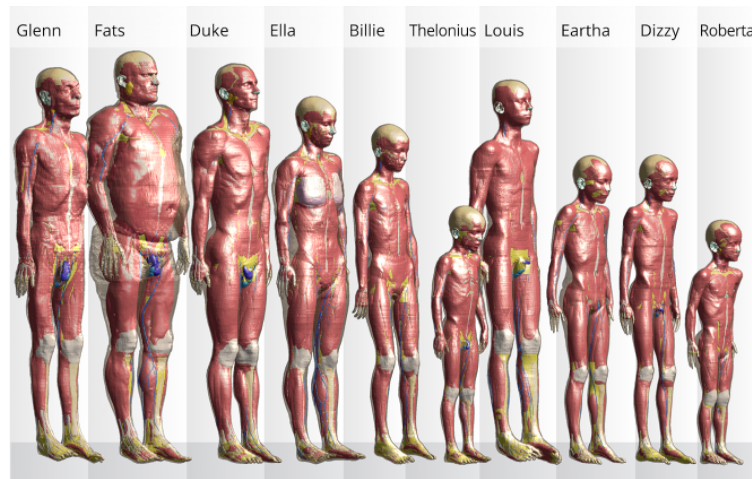


Figure 4.1: Virtual population models acquired with magnetic resonance imaging. (Gosselin et al., 2014)

Out of all adult models, Ella was chosen for this part of simulations. Ella is a 26 year old woman and was preferred to 34 year old Duke considering computational parameters such as memory allocated when attempting to reconstruct multiple images. Ella's body is smaller than Duke's.

4.1.2 Mesh

Tetrahedral finite element mesh out of the human model were calculated using primarily the CGAL C++ numerical library via the iso2mesh matlab/octave wrapper. A section of the body that contains the liver was extracted, as shown in figures 4.2 and 4.3.

The resulting mesh out of the part of the body that contains the liver is shown in figure 4.4. It consists of 227722 tetrahedra and 44438 points between them. This is a relatively modest mesh occupying only 13 MB of memory.

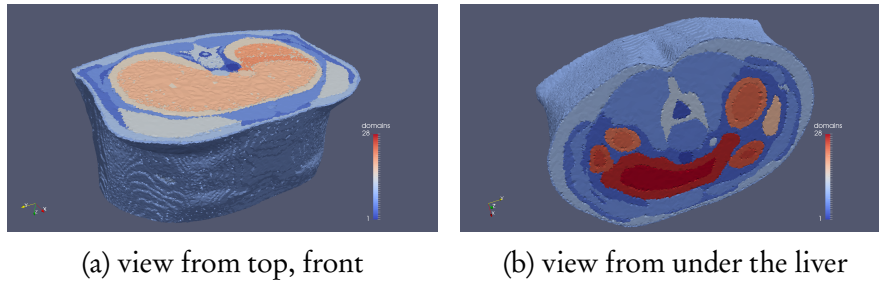


Figure 4.2: Image segmentation of liver section. 28 different tissues are included in this section.

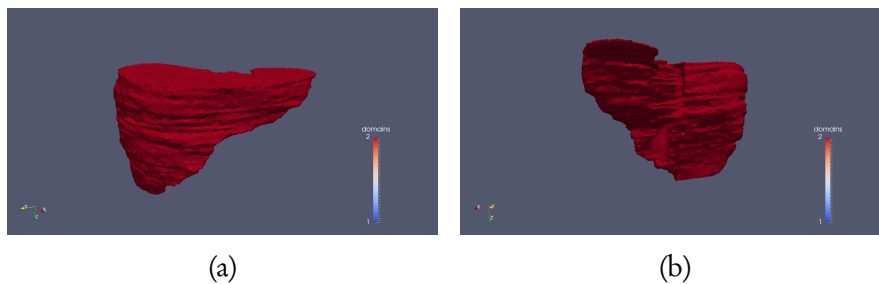


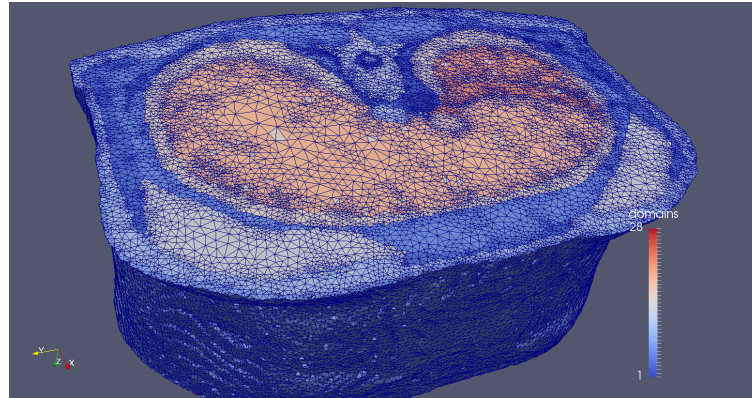
Figure 4.3: Human liver model as imaged by the magnetic resonance topographer.

4.2 Model design

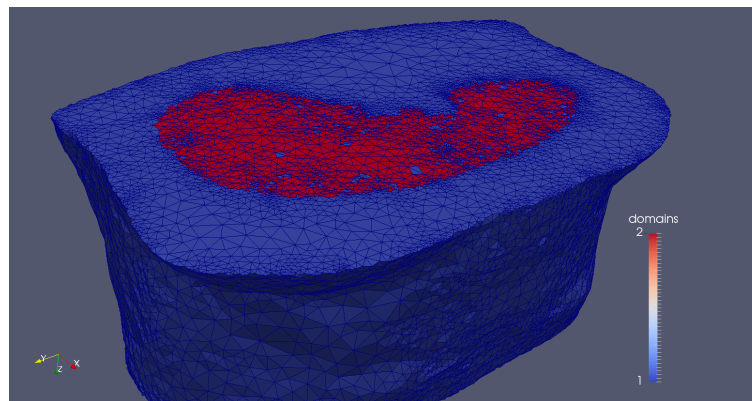
4.2.1 Electrodes placement

Electrodes were assumed points without size. In order to fit a number of electrodes onto the surface points of the realistic human model, we came up with the following algorithm

1. Extract all points of the cells on the outer surface
2. Find belt of points at height $z_0 \pm \text{tolerance}$
3. Calculate center of mass coordinates
4. From the points in the belt find point with maximum distance from the center
5. Define circle using the center of mass and the maximum distance found from the center
6. Define a number of points linearly on the circle equal to the desired number of electrodes



(a) Model tessellation. Mesh is finer near the domain boundaries.



(b) Tessellation comprising of only two different domains, one of them is the liver.

Figure 4.4: Model tessellation created with the Delaunay algorithm.

7. For each point on the circle, find the point on the belt with the minimum distance. Attach an electrode to this point on the model.

Numerical library VTK was used for the extraction of the surface points and the calculation of the center of the mass. The algorithm was implemented in Python. A simplified process is illustrated in figure 4.6.

4.2.2 Target area properties

The tumor which acts as the target of the therapy process was placed at the top part of the liver. It was designed as a spherical domain with electrical conductivity that is different from the background conductivity of the liver tissue. The coordinates of its center are (111,60,95) mm. Its radius is 5, so that it is well placed inside the liver. The entire model dimensions are x-range (8.41 to 197) mm, y-range (3.49 to 290);mm, z-range (0 to 115);mm. The origin of the computational domain

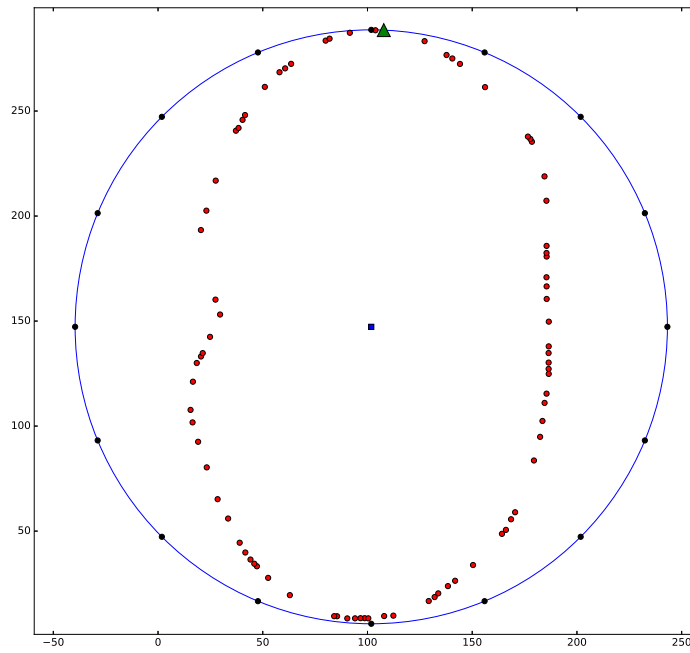


Figure 4.5: Create starting points in circle around realistic human model.

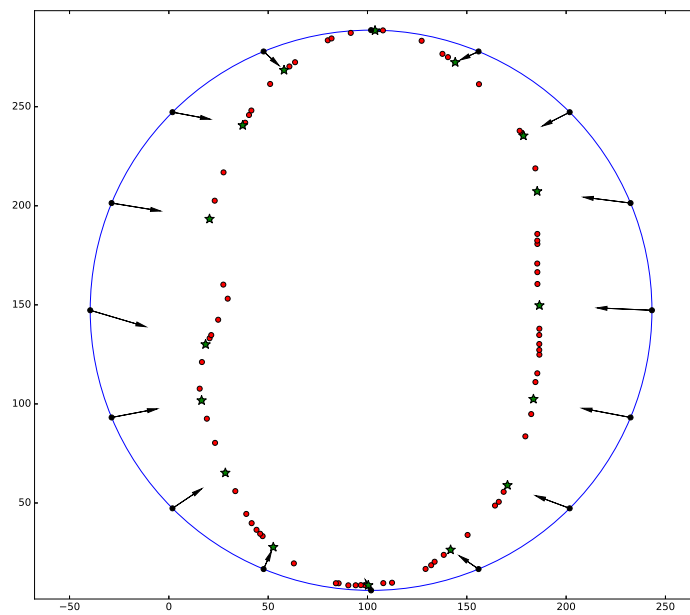


Figure 4.6: Model points with minimum distance from the starting points are selected for electrodes to be placed.

is at the bottom left. Images of the model before the application of the electrical impedance tomography are shown in figure 4.7.

4.3 Reconstruction results

4.3.1 Forward solution

By solving the forward problem we mean solving the Laplace equation for the static electrical field generated during the electrical impedance tomography. For 16 electrodes, the equation is solved 8 times, since the stimulation is generated from two different electrodes each time, as described in chapter 1. EIDORS offers several different stimulation patterns; here we used an adjacent pattern generated between nearby electrodes. The current amplitude of the stimulating electrodes was set at 10 mA and the contact impedance of each electrode at 10^{-3} Ohm.

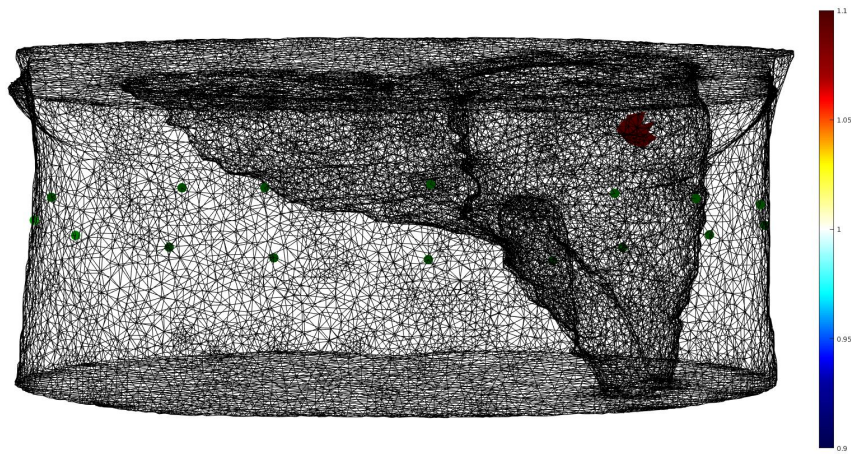
The solution of the forward problem when the stimulation is generated from the first pair of electrodes is shown in figure 4.8. The tumor can be imaged when subtracting the inhomogeneous solutions from the homogeneous.

4.3.2 2D reconstruction

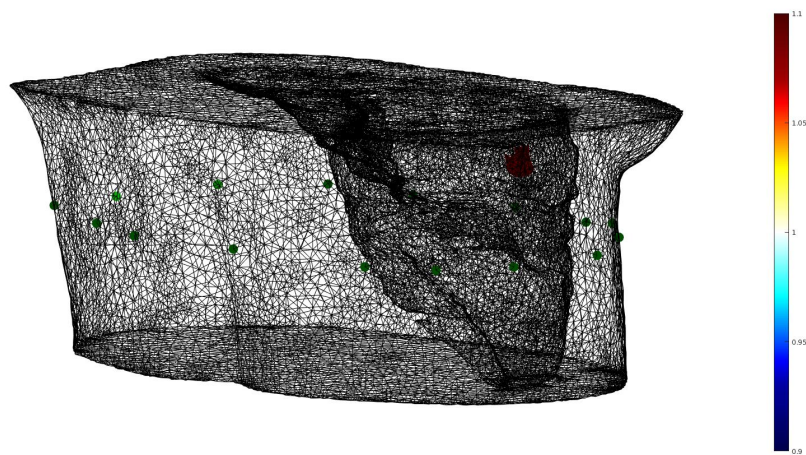
A two-dimensional test is presented in figure 4.9. The conductivity of the homogeneous background was set to 1 S/m, while the conductivity of the target was set at 1.1 S/m. The noser regularization scheme was used, along with a hyperparameter of 0.02. The absolute value of the reconstructed conductivity depends highly on the value of the hyperparameter. Generally, precision increases with low hyperparameter, but a very small value of the hyperparameter may results in overfitting.

$\sigma_{expected}$	$\sigma_{reconstructed}$	error %
1.10	1.07	2.64

Table 4.1: Mean expected and reconstructed conductivity value.

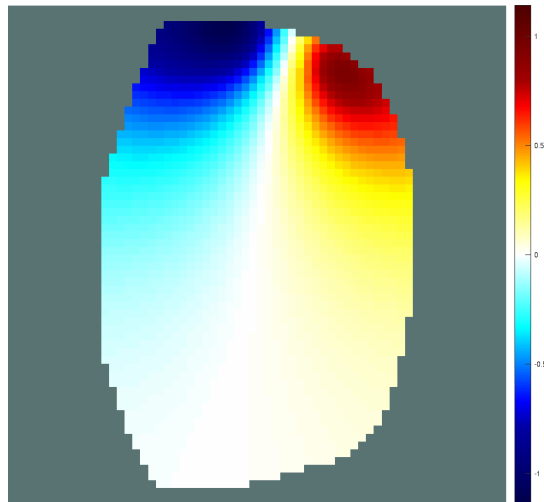


(a)

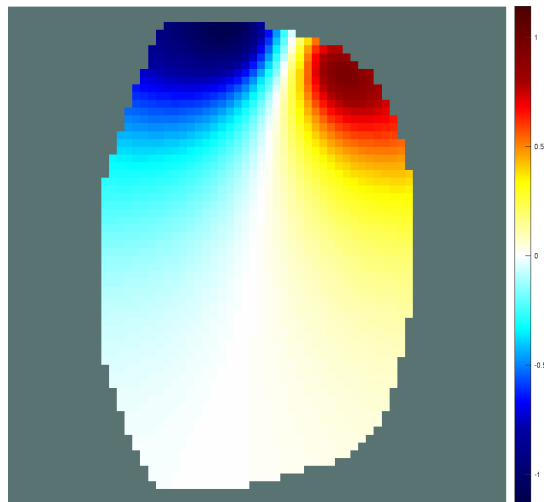


(b)

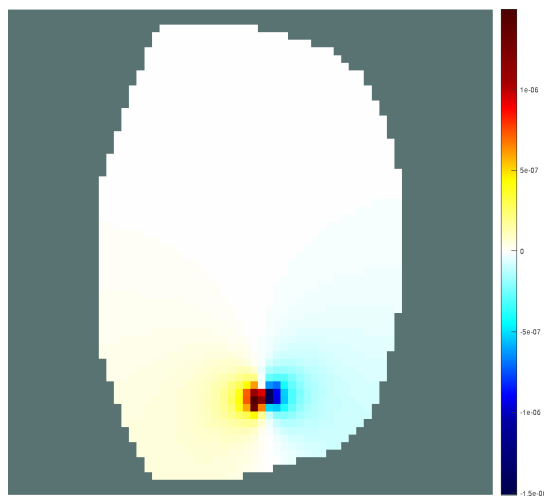
Figure 4.7: Tumor created in the top part of the liver. 16 electrodes are placed at almost equal distances around.



(a) Homogeneous model

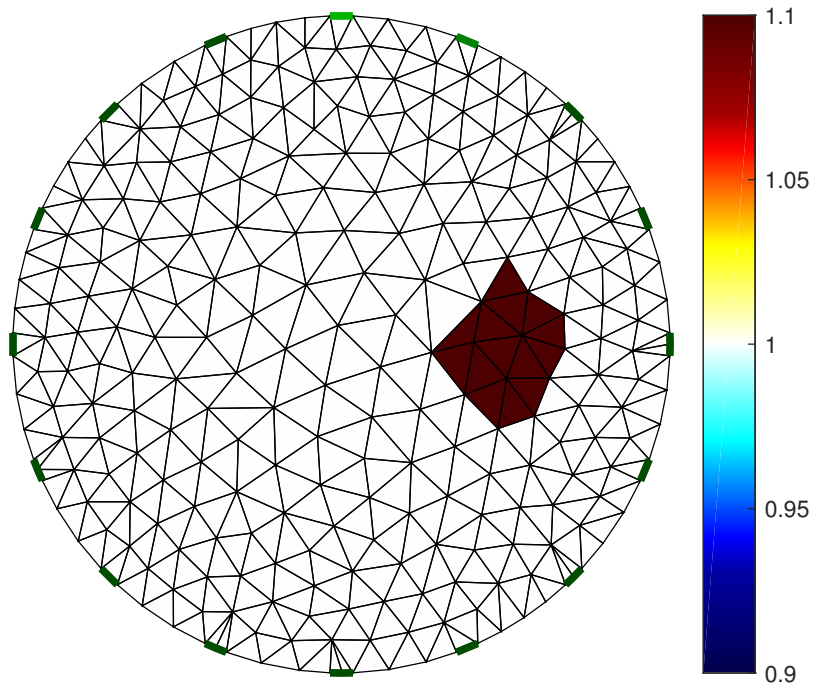


(b) Inhomogeneous model

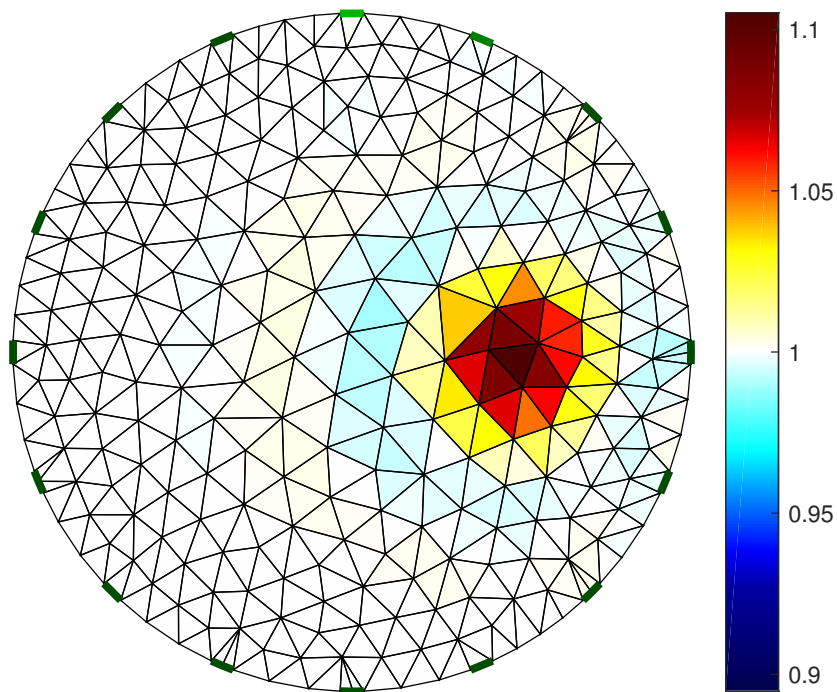


(c) Difference between inhomogeneous and homogeneous solutions

Figure 4.8: Electrical potential distribution calculated by solving the Laplace equation.



(a) Expected conductivity image



(b) Reconstructed conductivity image

Figure 4.9: Reconstruction of conductivity image in a two-dimensional model.

4.3.3 Single instance reconstruction

As a preliminary single instance evaluation, a simplified case was designed. The conductivity of the homogeneous background was set to 1 S/m. For the inhomogeneous case, the target area was assumed to be more conductive, thus the conductivity of the spherical tumor was set to be 0.1 S/m on top of the background. The resulting reconstruction of the image when applying difference imaging is shown in figure 4.10. The method is implemented by applying the Gauss-Newton algorithm for one step to find the difference in the conductivity, $\Delta\sigma$. For the inhomogeneous case, all tissues were considered to have the same background conductivity apart from the target area.

For the reconstruction algorithm the hyperparameter for the regularization was set at 10^{-4} . Several different regularization schemes were tested. Noser regularization, as described in chapter 3, was preferred due to its performance on three-dimensional grids.

4.3.4 Multiple reconstruction during ablation

To simulate the around 10 min application of the ablation treatment, we used experimental values for the conductivity as presented in section 1.1.3 to solve the forward problem and subsequently reconstruct the image for every minute of the treatment. The used values for the conductivity of the under ablation target area, which were measured during microwave ablation on bovine liver, are shown in table 4.2 along with the values for the conductivity from the resulted reconstructed images.

Time (min)	$\sigma_{expected}$	$\sigma_{reconstructed}$	error %
0	1.79	1.79	0
1	1.71	1.72	0.74
2	1.66	1.68	1.20
3	1.63	1.65	1.48
4	1.59	1.62	1.86
5	1.55	1.58	2.23
6	1.43	1.48	3.36
7	1.38	1.43	3.83
8	1.34	1.40	4.20
9	1.30	1.36	4.57
10	1.26	1.32	4.94

Table 4.2: Mean expected and reconstructed values for tumor conductivity.

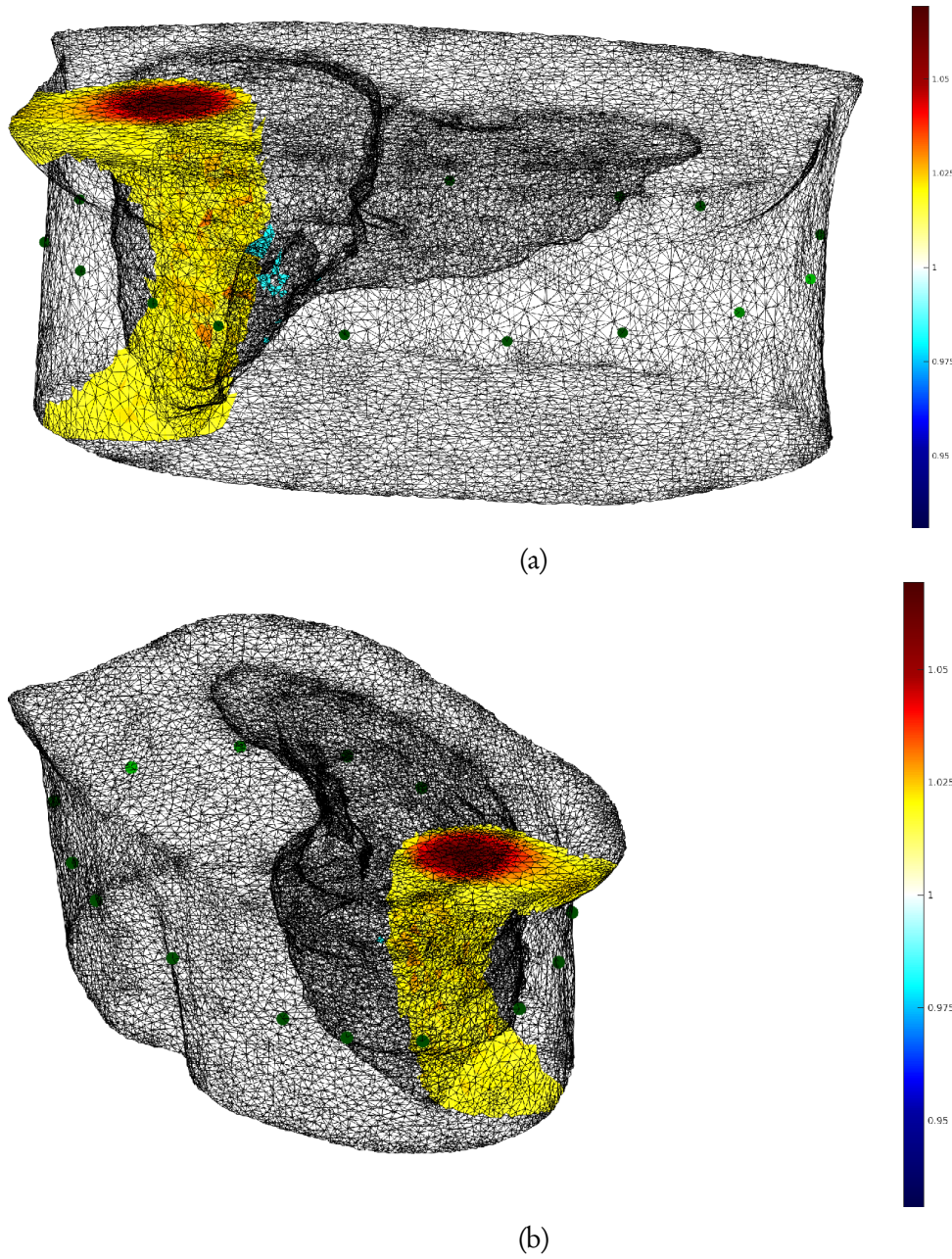


Figure 4.10: Image reconstruction of model with conductive tumor tissue

The rest of the tissues in the model were considered to be homogeneous with the same background conductivity of 1.79 S/m. Difference imaging with reference to the homogeneous case was applied for every minute of the treatment: Each measured (assumed) potential V_i was evaluated against the potential in the homogeneous model, V_{hom} for every minute i .

$$\Delta\sigma_i = \text{DifferenceImaging}(V_i, V_{hom}) \quad (4.1)$$

The difference in conductivity was then added to the homogeneous image to produce the reconstructed one,

$$\sigma_i = \sigma_{hom} + \Delta\sigma_i \quad (4.2)$$

The relevant hyperparameter was set at 10^{-10} and Noser regularization scheme was used for each of the total 10 reconstructions. To calculate the values of conductivity from the reconstructed image the average of each cell that belongs entirely to the target area was taken.

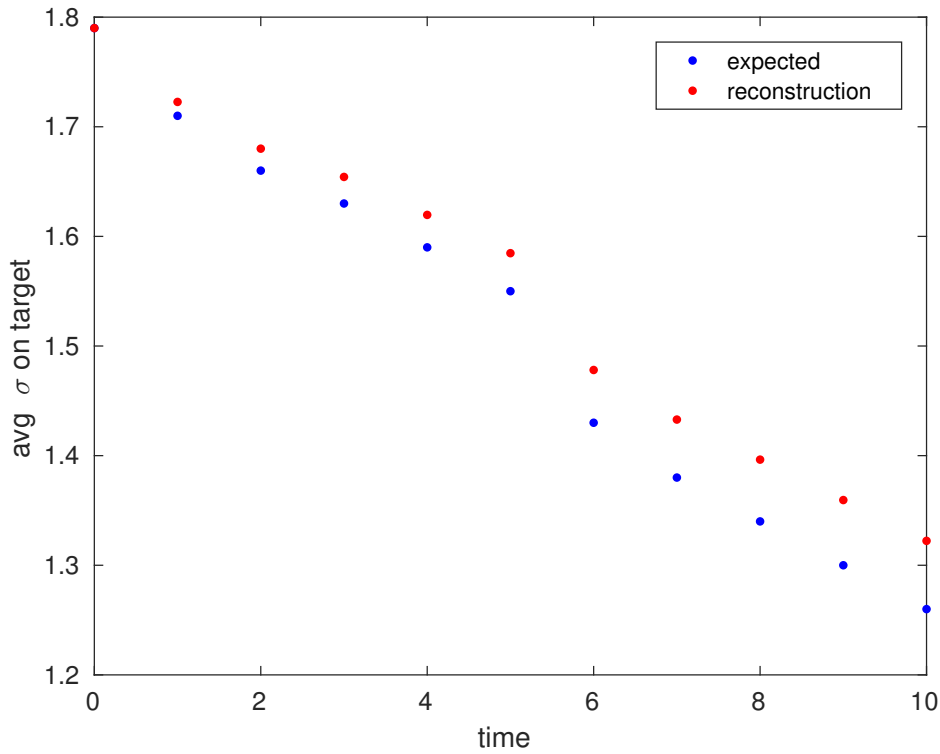


Figure 4.11: Average expected and reconstructed conductivity on target area.

5

Discussion

This study demonstrated the feasibility to perform real-time imaging of the application area during microwave ablation using electrical impedance tomography. There are a number of ways, some of which are presented in this chapter, in which the results of an *in silico* imaging analysis can be improved – including real voltage measurements from actual tomography. Nevertheless, the results of this work indicate that it is possible to achieve quality imaging and reliable real-time evaluation of the target area during microwave ablation.

5.1 On the forward problem

For the calculation of the voltages on the electrodes around the model EIDORS' forward solver was used primarily. Its results were validated against an own implementation of the finite element method for the static electrical field that was developed in C++ for this study. Two options for the geometry of the cells were offered by EIDORS: Linear first order and quadratic second order elements.

Since second order tetrahedra consist of 10 degrees of freedom compared to 4 for first order elements, they demand a considerable amount of computational resources. Even more, reconstruction algorithms in EIDORS currently do not support second order elements. As such, the additional 6 nodes per element in a second order mesh only improve the solution in the first 4, i.e the solution at the vertices of the tetrahedra. One has the possibility to use second order mesh for the forward problem to achieve better solution, but the second order elements do not take part in the reconstruction.

We compared the reconstructed image when the forward solution was obtained with second order to the one obtained with first order elements. A comparison analysis is not presented here but since our primary aim was to overcome the ill-conditioning of the inverse problem, we decided that higher order elements for the forward problem were unnecessary. This is even more evident when considering that the resulting solution from the FEM can be substantially improved by using a finer (first order) mesh in the first place.

5.2 On the model design

The human model that was used is extremely realistic, since it was obtained at 1mm resolution with magnetic resonance imaging. Clinical application parameters for the application of the MWA were taken into consideration when designing the target area and the functionality of the electrodes.

The target was designed as a spherical area of radius 5mm, bearing in mind that during microwave ablation the surrounding area of 20mm is directly affected and ablated at temperatures over 100 °C. The values for the electrical conductivity, as obtained for the bovine liver should describe accurately the whole area of 20mm around the antenna during the ablation at 2.45 GHz.

The 16 electrodes were assumed to contact only one point of the mesh each. For a future improvement of the resulting reconstructed image, one could use two zones (or even three) of surrounding electrodes at different heights to obtain a more accurate result.

This algorithm described in section 4.2.1 for the attachment of the electrodes to the model is robust against many model geometries (including primitives), however the electrodes may not end up to be absolutely equidistant. Small variations at the distances between them are apparent in the resulting figures. However, we assume that small variations in the distances of the electrodes are inevitable anyway during

an actual application of the tomography, and thus we opted not to optimize further their positions.

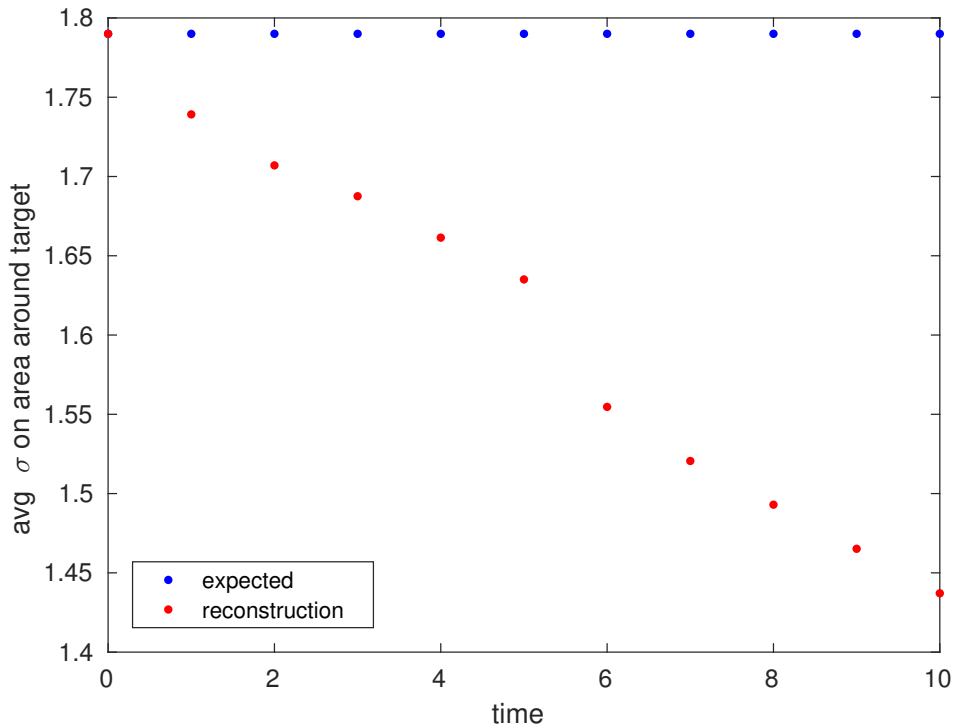


Figure 5.1: Average expected and reconstructed conductivity on healthy area around the target area.

5.3 On the reconstructed image

We used EIDORS' difference imaging algorithms for the image reconstruction. Difference imaging assumes a homogeneous distribution of the potential as a reference solution. As observed in the values obtained for the conductivity at figure 4.11, the error from the expected value increases for reconstructed images that differ considerably from the homogeneous reference background. The more inhomogeneous the reconstructed image is, the more its error from the expected value increases.

That is not surprising, since the assumption for the Gauss-Newton algorithm is that the difference in conductivity $\Delta\sigma$ is a relatively small number. After the application of microwave ablation for 10 minutes the resulting reconstructed image is shown in figure 5.2.

It is important to evaluate how focused the treatment is and how much damage potentially causes to healthy tissues. The optimal result would be to ablate as

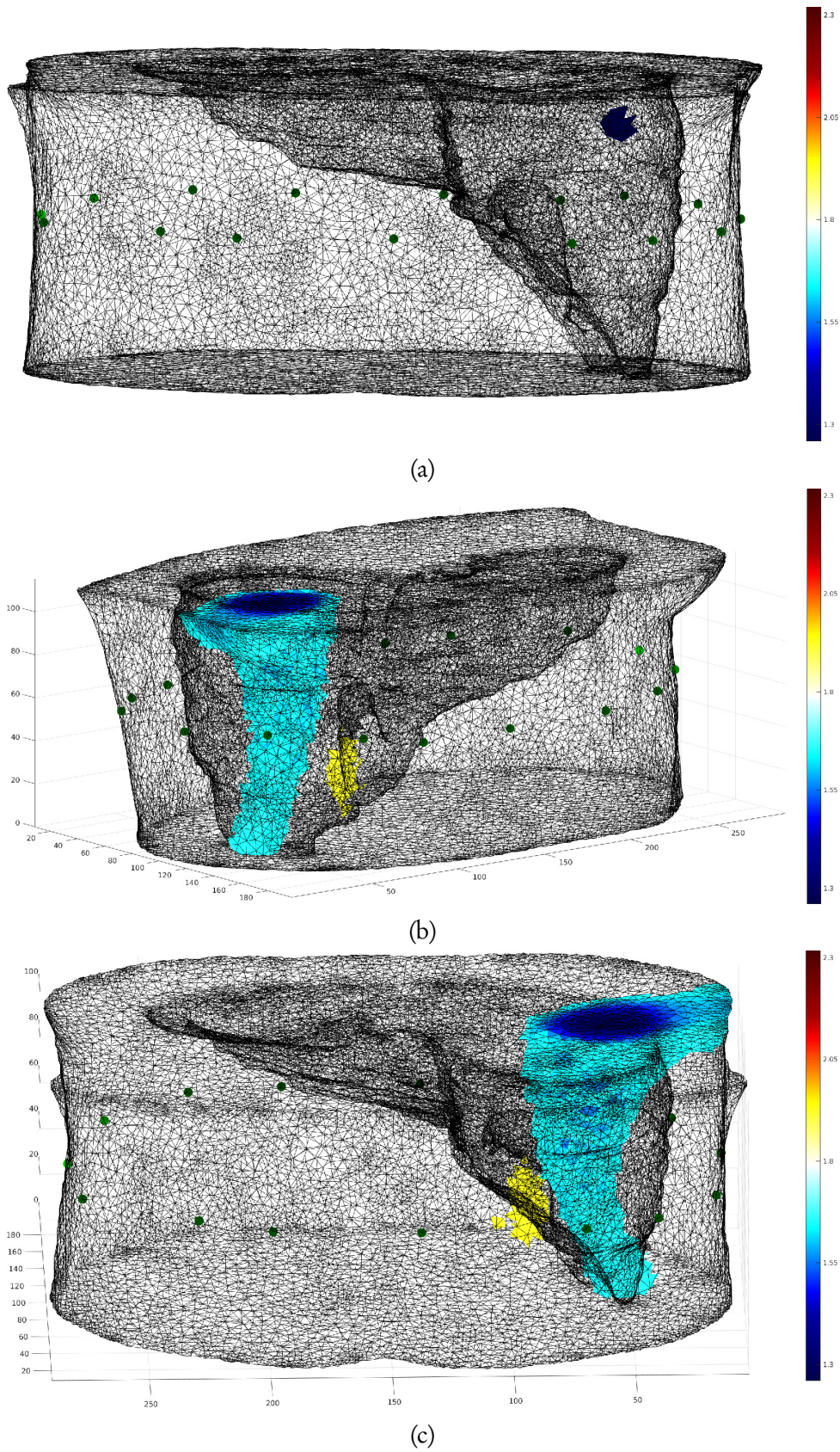


Figure 5.2: Reconstruction of target area at the end of the treatment compared to the expected.

much as possible –if not all– of the cancerous area, and as little as possible of the surrounding cells. To evaluate the spatial accuracy of the microwave ablation to the area around the tumor we measured the average at a spherical area of radius 20mm around the target area without the target area. As it can be seen in figure 5.1 healthy tissue is affected but to a much lesser extent. Average conductivity drops at around $1.45 S/m$, whereas in the target it dropped at exactly $1.32 S/m$.

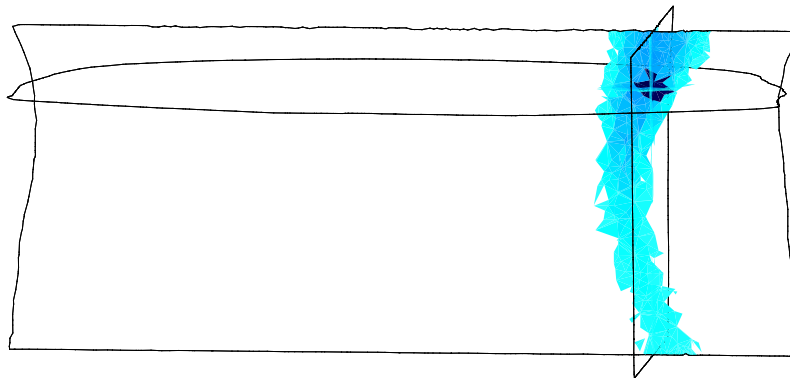


Figure 5.3: 3D slice of the reconstructed image. Hyperparameter: $1e-4$.

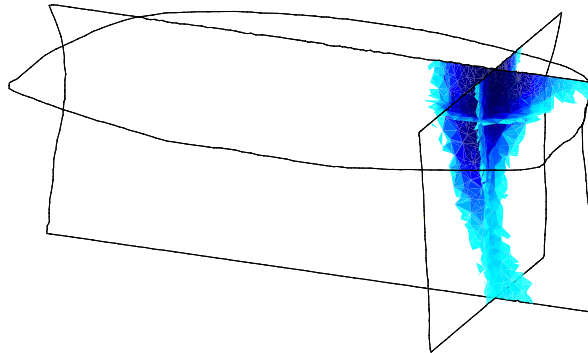


Figure 5.4: 3D slice of the reconstructed image. Hyperparameter: $1e-10$.

It is worth pointing out the effect that the particular geometry chosen has on the final outcome. A relatively small section of the human body was isolated, so that contains the entire liver. By assessing the reconstructed image in figure 5.4, it

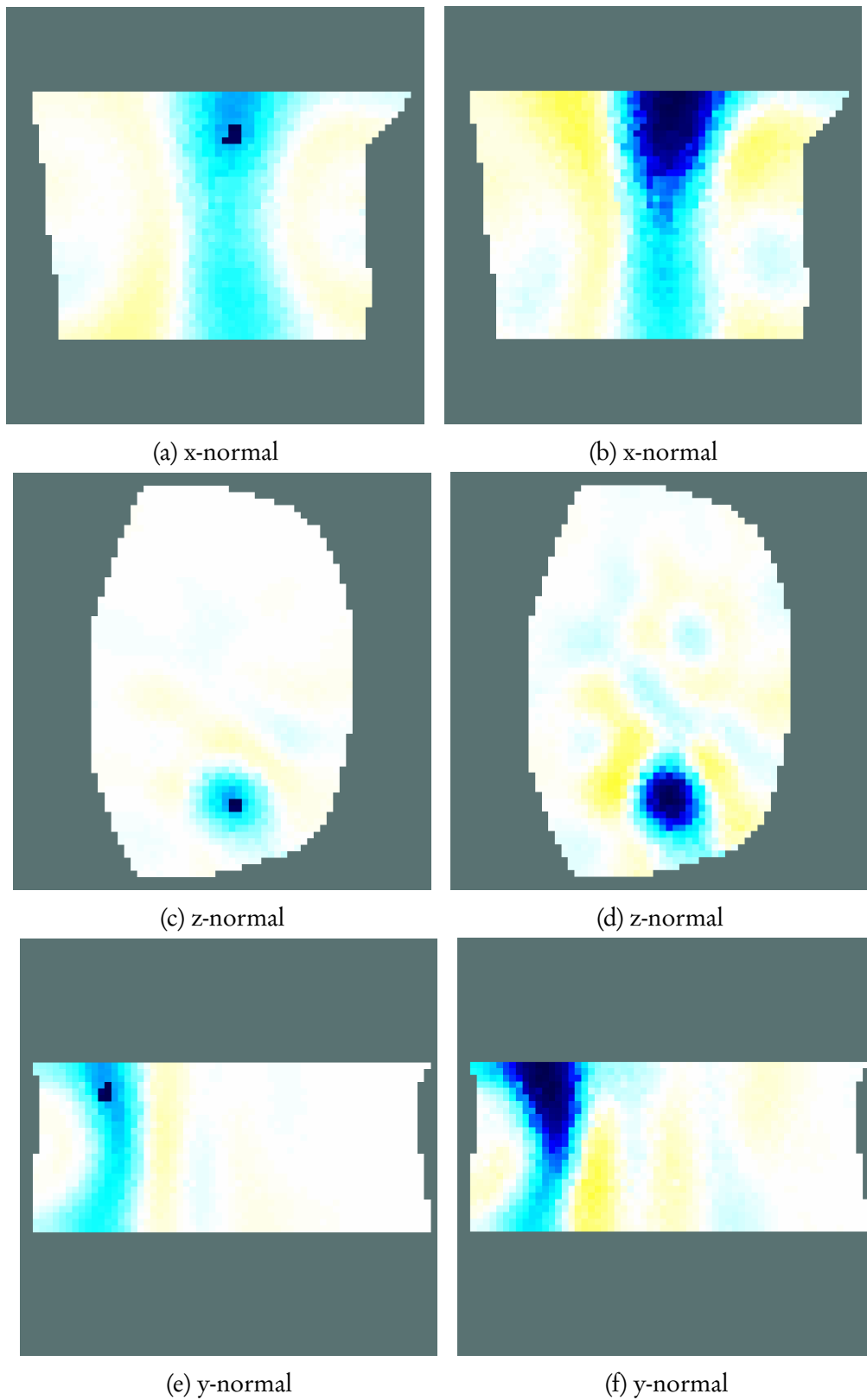


Figure 5.5: Slices of the reconstructed image for each axis. Images on the left column were generated with hyperparameter value $1e-4$, whereas images on the right column were generated with hyperparameter $1e-10$.

is apparent the axial vertical effect the height of 115mm has. Such an outcome it is expected, since the height of the model is relatively small compared to its horizontal width (190mm for the x-axis and 286mm for the y-axis). This effect confirms the correctness of the reconstruction algorithms that were used and makes future work highly promising.

Bibliography

- Adler, A. and W. R. B. Lionheart (2006). “Uses and abuses of EIDORS: an extensible software base for EIT”. In: *Physiological Measurement* 27.5.
- Ahmed, M. et al. (2011). “Principles of and Advances in Percutaneous Ablation”. In: *Radiology* 258.2.
- Andler, A. and R. Guardo (1996). “Electrical impedance tomography: regularised imaging and contrast detection”. In: *IEEE Transactions on Medical Imaging* 15, pp. 170–179.
- Balay, Satish et al. (2016). *PETSc Web page*. <http://www.mcs.anl.gov/petsc>. URL: <http://www.mcs.anl.gov/petsc>.
- Brace, C. L. (2009). “Microwave Ablation Technology: What Every User Should Know”. In: *Current problems in diagnostic radiology* 38, pp. 61–67.
- Cheney, M. Q. et al. (1990). “NOSER: An algorithm for solving the inverse conductivity problem”. In: *International Journal of Imaging Systems and Technology* 2, pp. 66–75.
- Chu, K. F. and D. E. Dupuy (2014). “Thermal ablation of tumours: biological mechanisms and advances in therapy”. In: *Nature Reviews Cancer* 14, pp. 199–208.
- Elman, H, D. Silvester, and A. Wathen (2005). *Finite Elements and Fast Iterative Solvers with applications in incompressible fluid dynamics*. Oxford University Press, pp. 1–415.
- Gosselin, Marie-Christine et al. (2014). “Development of a New Generation of High-Resolution Anatomical Models for Medical Device Evaluation: The Virtual Population 3.0”. In: *Physics in Medicine and Biology* 59 (18), pp. 5287–5303.
- Graham, B. M. (2007). “Enhancements in Electrical Impedance Tomography (EIT) Image Reconstruction for 3D Lung Imaging”. PhD thesis. University of Ottawa.
- Holder, DS. (2005). *Electrical Impedance Tomography: Methods, History and Applications*, pp. 65–103.
- Hughes, T.J.R. (1987). *The Finite Element Method*. Prentice Hall, pp. 1–415.

- Irina, VL, VL Kirill, and OE Rinat (2005). “Real-time optoacoustic monitoring of temperature in tissues”. In: *Journal of Physics D: Applied Physics* 38, pp. 2633–2639.
- Ji, Zhen and Christopher L Brace (2011). “Expanded modeling of temperature-dependent dielectric properties for microwave thermal ablation”. In: *Physics in Medicine and Biology* 56, pp. 5249–5264.
- Lopresto, Vanni et al. (2012). “Changes in the dielectric properties of ex vivo bovine liver during microwave thermal ablation at 2.45 GHz”. In: *Physics in Medicine and Biology* 57, pp. 2309–2327.
- Lubner, M. G. et al. (2010). “Microwave tumor ablation: mechanism of action, clinical results, and devices”. In: *Journal of Vascular and Interventional Radiology* 21.8, pp. 192–203.
- Nikfarjam, M., V. Muralidharan, and C. Christophi (2005). “Mechanisms of Focal Heat Destruction of Liver Tumors”. In: *Journal of Surgical Research* 127, pp. 208–203.
- Polydorides, Nick (2002). “EIDORS: Towards a community-based extensible software base for EIT”. PhD thesis. University of Manchester Institute of Science and Technology.
- Polydorides, Nick and William R B Lionheart (2002). “A Matlab toolkit for three-dimensional electrical impedance tomography: a contribution to the Electrical Impedance and Diffuse Optical Reconstruction Software project”. In: *Measurement Science and Technology* 13.12.
- Teschner, E., M. Imhoff, and S. Leonhardt (2011). *Electrical Impedance Tomography: The realisation of regional ventilation monitoring*.
- The CGAL Project (2016). *CGAL User and Reference Manual*. 4.9. CGAL Editorial Board. URL: <http://doc.cgal.org/4.9/Manual/packages.html>.
- Webster, JG (1990). *Electrical Impedance Tomography*, pp. 1–224.
- Wi, H. et al. (2015). “Real-time Conductivity Imaging of Temperature and Tissue Property Changes During Radiofrequency Ablation: An ExVivo Model Using-Weighted Frequency Difference”. In: *Bioelectromagnetics* 36, pp. 277–286.
- Wright, A. S., F. T. Lee, and D. M. Mahvi (2003). “Hepatic microwave ablation with multiple antennae results in synergistically larger zones of coagulation necrosis”. In: *Annals of surgical oncology* 10, pp. 275–283.